AGU PUBLICATIONS

JGR

Journal of Geophysical Research: Oceans

RESEARCH ARTICLE

10.1002/2013JC008999

Special Section:
Canada's Three Oceans Project, A Canada's International Polar Year Initiative

Deterioration of perennial sea ice in the Beaufort Gyre from 2003 to 2012 and its impact on the oceanic freshwater cycle

R. A. Krishfield[1], A. Proshutinsky[1], K. Tateyama[2], W. J. Williams[3], E. C. Carmack[3], F. A. McLaughlin[3], and M.-L. Timmermans[4]

[1]Woods Hole Oceanographic Institution, Woods Hole, Massachusetts, USA, [2]Department of Civil and Environmental Engineering, Kitami Institute of Technology, Kitami, Hokkaido, Japan, [3]Fisheries and Oceans Canada, Institute of Ocean Sciences, Sidney, British Columbia, Canada, [4]Yale University, New Haven, Connecticut, USA

Key Points:
- Sea ice in the Beaufort Gyre became thinner and largely homogenous after 2007
- Total summer freshwater increased until 2010 and has decreased slightly since
- Thick sea ice declined from nearly 10 to 4% of the total summer freshwater budget

Correspondence to:
R. A. Krishfield,
rkrishfield@whoi.edu

Citation:
Krishfield, R. A., A. Proshutinsky, K. Tateyama, W. J. Williams, E. C. Carmack, F. A. McLaughlin, and M.-L. Timmermans (2014), Deterioration of perennial sea ice in the Beaufort Gyre from 2003 to 2012 and its impact on the oceanic freshwater cycle, *J. Geophys. Res. Oceans*, *119*, 1271–1305, doi:10.1002/2013JC008999.

Received 1 APR 2013
Accepted 13 JAN 2014
Accepted article online 16 JAN 2014
Published online 22 FEB 2014

Abstract Time series of ice draft from 2003 to 2012 from moored sonar data are used to investigate variability and describe the reduction of the perennial sea ice cover in the Beaufort Gyre (BG), culminating in the extreme minimum in 2012. Negative trends in median ice drafts and most ice fractions are observed, while open water and thinnest ice fractions (<0.3 m) have increased, attesting to the ablation or removal of the older sea ice from the BG over the 9 year period. Monthly anomalies indicate a shift occurred toward thinner ice after 2007, in which the thicker ice evident at the northern stations was reduced. Differences in the ice characteristics between all of the stations also diminished, so that the ice cover throughout the region became statistically homogenous. The moored data are used in a relationship with satellite radiometer data to estimate ice volume changes throughout the BG. Summer solid fresh water content decreased drastically in consecutive years from 730 km^3 in 2006 to 570 km^3 in 2007, and to 240 km^3 in 2008. After a short rebound, solid fresh water fell below 220 km^3 in 2012. Meanwhile, hydrographic data indicate that liquid fresh water in the BG in summer increased 5410 km^3 from 2003 to 2010 and decreased at least 210 km^3 by 2012. The reduction of both solid and liquid fresh water components indicates a net export of approximately 320 km^3 of fresh water from the region occurred between 2010 and 2012, suggesting that the anticyclonic atmosphere-ocean circulation has weakened.

1. Introduction

The Beaufort Gyre (BG) is a unique circulation component within the Arctic Ocean physical environment with a set of specific atmospheric, sea ice, and oceanic conditions that are interrelated with pan-Arctic as well as global climate systems [*Proshutinsky et al*., 2002, 2009, 2012; *Dukhovskoy et al*., 2004; *Carmack et al*., 2008; *Giles et al*., 2012, *Morison et al*., 2012]. Significant negative trends in observed Arctic sea ice extent and thickness over the past decade have prompted numerous discussions about the root causes and consequences of the rapidly changing Arctic climate [e.g., *Lindsay and Zhang*, 2005; *Overland et al*., 2008; *Kwok*, 2008]. Ocean changes in the BG (Figure 1) have been equally as prominent as the disappearing sea ice cover. For example, the BG accumulated more than 5000 km^3 of liquid fresh water in the period 2003–2012, an increase of approximately 25% [*Proshutinsky et al*., 2012] relative to the climatology of the 1970s. Not only does this have important consequences for the Arctic sea ice and ecosystems, but a fresh water release from the Arctic of this magnitude could trigger a salinity anomaly in the North Atlantic with magnitude comparable to the Great Salinity Anomaly (GSA) of the 1970s. GSAs can influence global climate by inhibiting deep wintertime convection that in turn can reduce the ocean meridional overturning circulation [*Vellinga et al*., 2008] and initiate cooling.

The fundamental governing dynamics operates the BG fresh water reservoir like a flywheel. Anticyclonic winds spin up the flywheel forcing accumulation of fresh water in the region. It is gradually released when the anticyclonic forcing weakens or changes sense of rotation to dominantly cyclonic wind forcing [*Proshutinsky et al*., 2002, 2009]. An atmospheric circulation regime with anticyclonic winds has dominated over the Arctic for at least 16 years (1997–2012), a departure from the typical 5–8 year pattern of alternation between anticyclonic and cyclonic regimes [*Proshutinsky et al*., 2012]. It may be that the BG fresh water reservoir will continue to accumulate fresh water and exceed anything observed in the past; alternatively a circulation shift, which would be expected from previous climatological behavior [*Proshutinsky and Johnson*, 1997], may initiate a period of fresh water release.

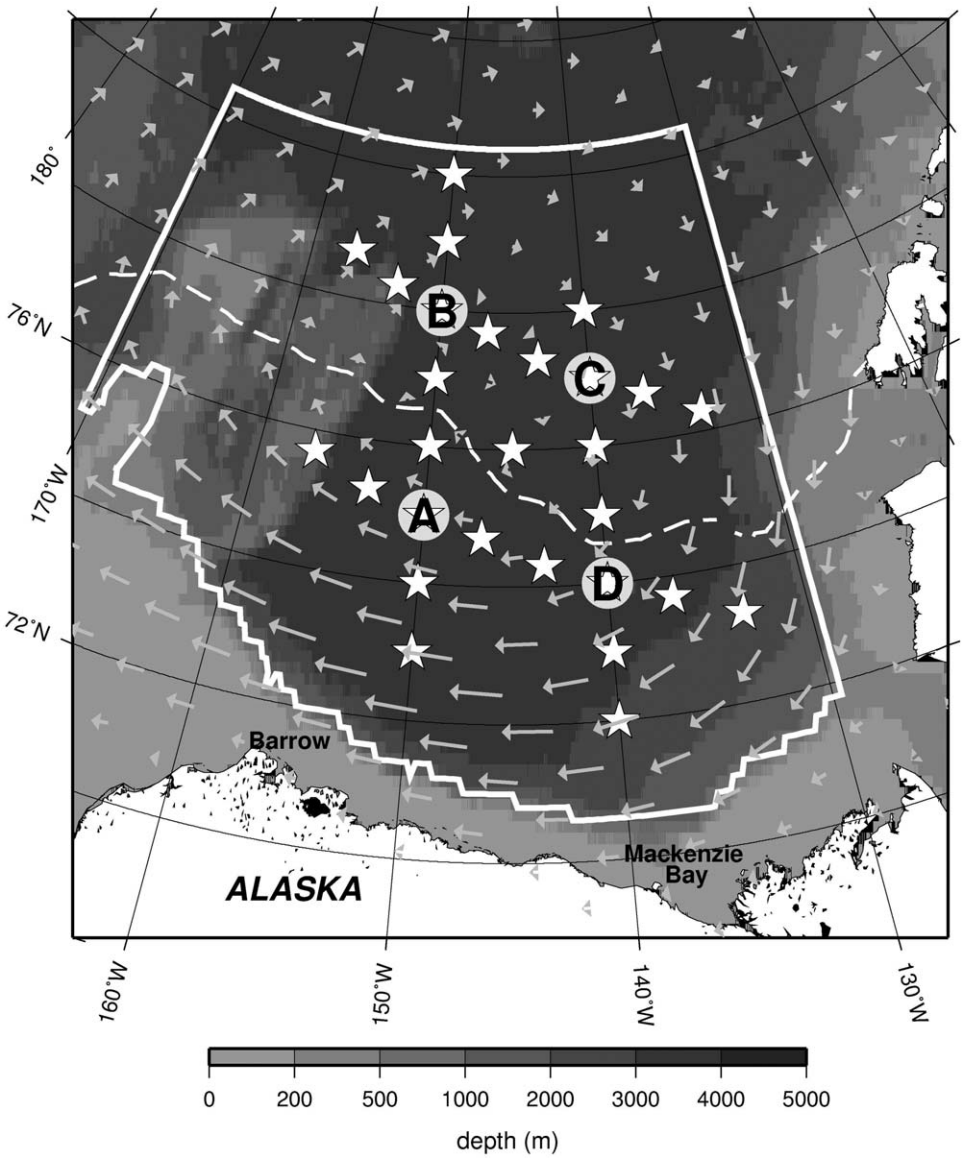

Figure 1. In this study, the BG is defined as the area (1.023×10^6 km^2) located between 70° and 80° N, 130° to 170° W with bathymetry deeper than 300 m (solid white line). Also indicated are the locations of BGOS moorings containing ULS (circles and letters), annual CTD stations (stars), mean climatological September ice edge from SSMI data (dashed white line), and mean 2003–2011 ice motion vectors (*Fowler and Tschudi* [2003, updated 2013]; arrows).

The goals of this paper are twofold: (a) to investigate changes of sea ice conditions in the BG using observations primarily from moored upward looking sonars, but also combined with satellite data, and; (b) to estimate the contribution of sea ice changes to changes in fresh water content in the BG and assess fresh water trends. The remainder of this paper is organized as follows: Section 2 provides some background information on different sea ice thickness measurement methods. Section 3 discusses the sources of data used in this paper. The methods of converting the upward looking sonar measurements into ice drafts and using satellite radiometer data to estimate regional ice draft are summarized in Section 4 (with details of the data processing procedures in Appendices A and B, respectively). Results of moored sonar observations are presented in Section 5 and the spatial representations based on the satellite algorithm in Section 6. In Section 7, a combination of the moored and satellite results is used to estimate solid fresh water content in the ice in the BG. Finally, in Section 8 the liquid fresh water component in the upper ocean interpolated from summer hydrographic stations is added to the solid component to calculate total BG fresh water content, and the physical environmental implications are discussed.

2. Background

A number of methods now exist to obtain either sea ice thickness, ice draft, or ice freeboard using electromagnetic detection through the ice surface, sonar below the ice cover, or altimetry radar from aircraft and satellites. Each of these methods includes some inherent uncertainties based on the accuracy of the sensors, footprint of the sensor beam, and errors associated with supplemental information (i.e., water column properties for speed of sound calculations and sea-level pressure for the under ice instrumentation, and reference level or geoid to be removed from the altimetry for aircraft and satellite methods).

Although satellite observations have the greatest spatial and temporal coverage, the large footprint of the sensor beam reduces the spatial resolution of the measurement and is a problem for determining ice thickness because it can vary greatly over short distances. Laser altimeter methods estimate ice freeboard [*Kwok et al*., 2012; *Laxon et al*., 2013], which is an order of magnitude smaller than thickness, so small errors in detecting freeboard can produce much greater errors when converted to ice thickness.

One method with a relatively small error utilizes self contained moored upward looking sonar (ULS) instruments to obtain year-round time series measurements of sea ice draft. Since the 1990s, several versions of these instruments have been utilized on bottom tethered moorings at a number of locations in the Arctic [e.g., *Melling et al*., 1995; *Fukamachi et al*., 2003; *Moritz and Ivakin*, 2012; *Hansen et al*., 2013] and Antarctic [*Strass*, 1998]. Though limited to discrete locations, these data provide the highest temporal resolution (0.5–1 hz), have a measurement footprint of less than 2 m in diameter (depending on the depth of the instrument), and can resolve some of the thinnest ($<$0.3 m) ice categories.

3. Data

In this study, we present long-term time series ice draft measurements from ULS moored in the BG of the Arctic Canada Basin, and detail the properties and changes in the ice cover at these specific locations. Satellite passive microwave radiometer data provide the basis to characterize regional variations in the ice cover. A pan-Arctic ice motion data that combines satellite and drifting buoys [*Fowler and Tschudi*, 2003, updated 2013] is also used to examine spatial variability.

3.1. In Situ Sonar Observations

Beginning in August 2003, model IPS-4 or IPS-5 ULS (manufactured by ASL Environmental Sciences in Canada) were deployed beneath the Arctic ice pack on either 3 or 4 (depending on year) BG Observing System (BGOS; *Proshutinsky et al*. [2009]; http://www.whoi.edu/beaufortgyre) bottom-tethered moorings in the BG of the Canada Basin (Figures 1 and 2) to obtain ice draft measurements. Annually on Joint Ocean Ice Study (JOIS) cruises [*McLaughlin et al*., 2010; *Williams*, 2010], the moorings were recovered, data retrieved from the instruments, and after servicing the systems were redeployed. All moorings were anchored in water deeper than 3500 m, and the ULS instruments were located in the top flotation sphere situated between 20 and 85 m beneath the ice cover (depending on actual mooring length and deployment depth).

The two mooring locations along 150° W longitude, named BGOS-A (at 75° N) and BGOS-B (at 78° N), have been continuously occupied since 2003 (Figure 1). Although BGOS-A has provided a continuous time series of ULS data since 2003, there are gaps in the data from BGOS-B due to instrument failures between summers 2005 to 2006 and 2009 to 2010. Mooring location BGOS-C (77° N, 140° W) was occupied and provided continuous ULS time series data from summer 2003 to 2009, before being discontinued. Mooring location BGOS-D (74° N, 140° W), first occupied in summer 2005, has provided a continuous ULS time series since summer 2006 due to instrument failure during the first year. Although the BGOS project is ongoing, this study examines the first 9 years of data ending in August 2012 (Table 1).

The ULS instrument measures the travel time of a directed 420 kHz beam (beamwidth 1.8°) to determine a range to the bottom surface of the ice (or sea surface in the absence of ice); pressure, temperature, and tilt are also sampled. At a nominal depth of 50 m, the footprint of the beam on the ice bottom is estimated to be about 2 m. Ice draft is determined from corrected range minus the corrected pressure of the transducer in the ULS (Figure 2). Tilt data are used to correct the range, and the pressure data are corrected for sound speed and density variations using temperature measurements taken every pressure period scaled with CTD data obtained at the beginning and end of each deployment [*McLaughlin et al*., 2010]. NCEP reanalysis

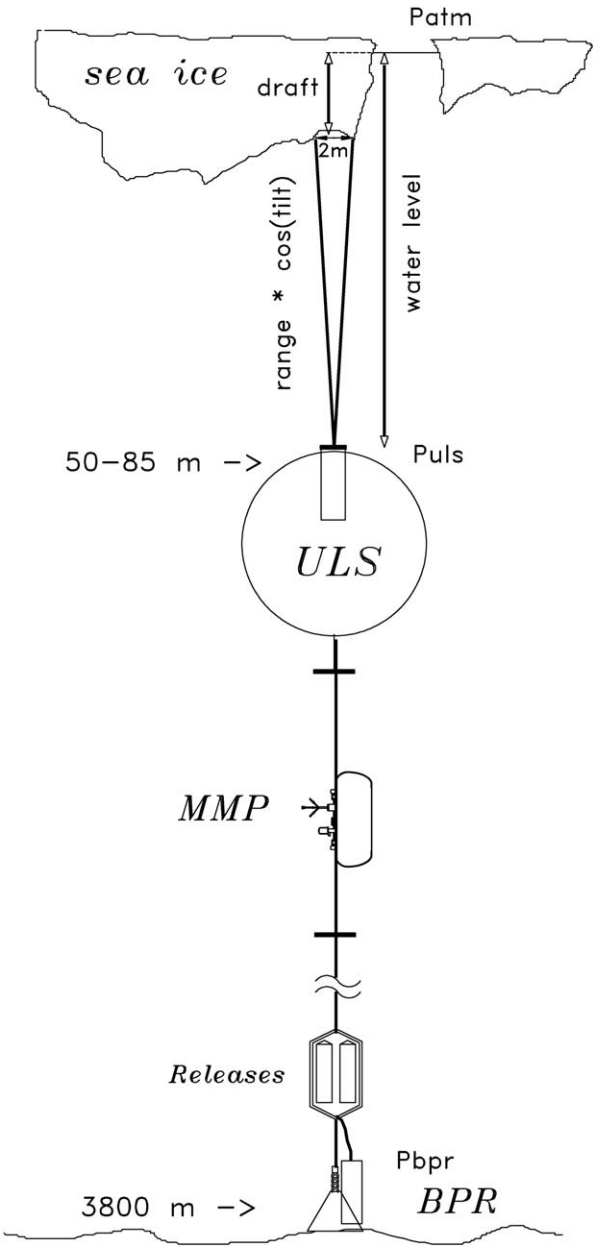

Figure 2. Schematic of BGOS moorings with ULS, McLane Moored Profiler (MMP), and Bottom Pressure Recorder (BPR) placement. Measured and computed parameters for estimating ice draft from ULS pressure, tilt, and range data are shown.

(http://www.cdc.noaa.gov/cdc/data.ncep.reanalysis.html) sea-level pressure (SLP) estimates are used to compensate for the atmospheric pressure. Raw draft can be in error by as much as 1 m before corrections for atmospheric pressure and speed of sound variations are applied. The sampling rate of the range pings is every 2 s, whereas seawater pressure and temperature are measured every 40 s. This sampling schedule typically provides over 15 million observations per mooring per year (Table 1) and after the seawater corrections are applied, the accuracy of each acoustic range measurement better than ±10 cm [*Melling and Riedel*, 1995]. Details of the ULS data processing scheme are described in Section 4 and in Appendix A.

In addition to providing speed of sound endpoints for the ice draft calculations, hydrographic profile data from 4 to 6 week JOIS surveys every summer between July and October from 2003 through 2012 [*McLaughlin et al*., 2010; *Williams*, 2010] are used for calculating liquid fresh water content. At least 30 and as many as 100 hydrographic CTD casts were conducted each year on JOIS cruises. Annual gridded fresh water estimates are constructed from these and other hydrographic data made available from other cruises.

3.2. Passive Microwave Radiometer Data

To resolve regional ice variability, we utilize a crude relationship with daily global microwave brightness temperature observed by the Advanced Microwave Scanning Radiometer—EOS (AMSR-E) mounted on NASA's *Aqua* satellite. Polar gridded products of AMSR-E brightness temperatures level 1B product and sea ice concentration level 2 product were provided by the IARC-JAXA (International Arctic Research Center—Japan Aerospace Exploration Agency) Information

Table 1. Summary of BGOS ULS Mooring Data Showing Location, Duration, and Number of Draft Measurements[a]

Mooring	°N	°W	Start	End	Days	Drafts
A	75	150	Aug 2003	Aug 2012+	3286	140801399
B	78	150	Aug 2003	Aug 2012+	3289	108205671
C	77	140	Aug 2003	Aug 2008	1810	77861698
D	74	140	Oct 2006	Aug 2012+	2173	93398059

[a]"+" Indicates data collection is ongoing.

System (IJIS) geoinformatics facility for satellite image analysis and computational modeling/visualization. The spatial resolution of these data are 10 km except the brightness temperatures of vertically and horizontally polarized 89 GHz which have 5 km resolution. This data set covers the period from July 2002 to October 2011.

4. Methods

The ULS measurements are used to calibrate a coarse algorithm to estimate sea ice thickness using satellite passive microwave observations, including the variability over the entire area of the BG. The solid (sea ice) fresh water component is computed and analyzed with respect to the liquid (seawater) fresh water component determined from hydrographic data, and its relevance to the total (solid plus liquid) fresh water budget in the region is examined.

4.1. Sea Ice Draft From Sonar Data

Ensuring comparability to other ice draft measurements determined from similar ULS [e.g., *Melling and Riedel*, 1995, 1996; *Melling et al*., 2005], the processing scheme used here largely follows the procedures employed by the ASL IPS Processing Toolbox [*Billeness et al*., 2004], except that here we developed a semiautomated method for determining the speed of sound correction factor (*beta*), which is manually tuned by selected parameters for each time series to produce a consistent ice draft product (where not explicitly stated "ice" refers to "sea ice" throughout the text). ASL Toolbox (version 1.02) recommended thresholds are used to remove spikes, but additional averaging of the raw ranges is also implemented. The averaging windows and selected other parameters used in the processing were fine-tuned by numerous iterations and visual inspections. Additional technical details on the processing routines are included in Appendix A.

After implementing the processing procedure, the estimated error of the individual ice draft measurements is better than $\pm$10 cm. This error may be exceeded during times of modest wave activity or long periods where no leads are available for calibrating *beta*. Usually waves can be clearly identified and removed and open water occurrences were frequent enough that confident *betas* could be determined. Due to significant variability, uncertainties associated with daily averages are nearly the same.

Statistics (number of observations, mean, minimum, maximum, median, standard deviation) for the 2 s time series data are computed at daily intervals for each mooring. The statistics calculated for ice draft also include the contributions of open water (ice draft = 0) and daily distributions of ice draft in 10 cm increments. These products provide the basis for the results described below.

4.2. Satellite-Based Sea Ice Draft Relationship

The spatial distribution of sea ice draft is a key parameter for understanding the evolution of sea ice in the BG. The moored ice draft time series provide high frequency and relatively precise information at the observation sites and adequately resemble the spatial distributions around those immediate areas; however, the data set provides information at only four locations, and it is uncertain how representative the sites are of the region of the BG as a whole (defined as 70–80° N, 130–170° W and with bathymetry exceeding 300 m, see Figure 1).

To provide more spatial detail over the entire BG, ice drafts at the mooring sites were used to tune an algorithm to estimate the spatial variability of ice draft over the region using relationships with AMSR-E passive microwave radiometer satellite data [*Tateyama et al*., 2013]. A detailed description of the algorithm development is provided in Appendix B. AMSR-E satellite passive microwave data were compared with in situ information from a shipboard Electro-Magnetic induction ice thickness profiler (EM) and a portable passive microwave radiometer system during summer cruises in the BG between 2009 and 2012 and relationships determined. The relationships classify between first-year (growing ice) and old ice and include overlap between classes. They are tuned with the in situ measurements of ice draft from the ULS data to minimize the statistical error, and produce spatial grids.

The resulting product consists of daily 5 km grids of ice drafts throughout the Arctic from May 2003 through May 2011 (the duration of the IJIS data set). Agreement between the satellite-based product and in situ observations are shown in scatterplots (Figure 3) of daily average ULS data versus daily values derived using

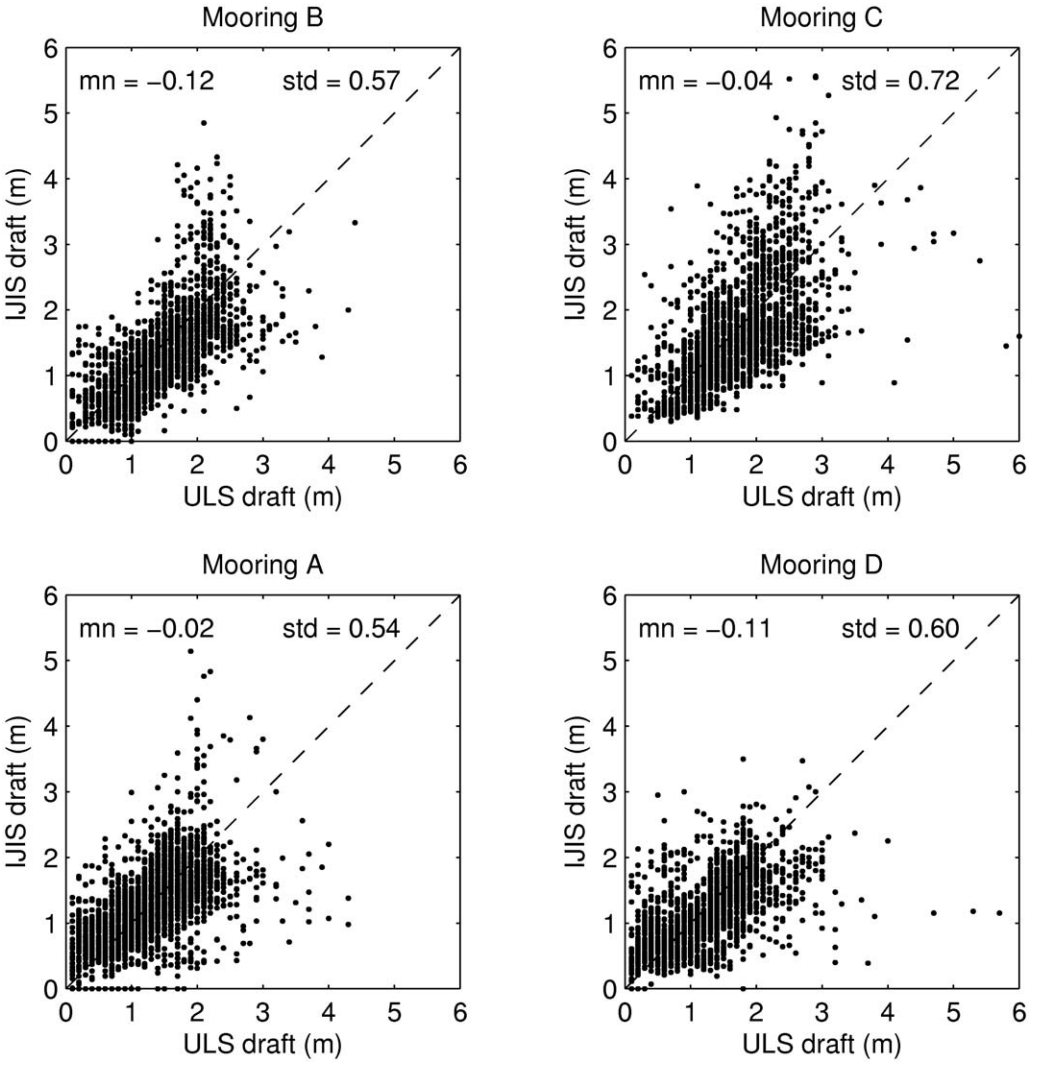

Figure 3. Scatter diagrams of daily ice drafts for each mooring site: ULS data versus daily ice drafts estimated from AMSR-E data using the IJIS algorithm. The means and standard deviations of the differences of the IJIS estimates from the ULS estimates are also indicated for each mooring. The median percent difference from the ULS estimates for all moorings is 27%.

the revised algorithm for each mooring location. Overall, the IJIS algorithm appears to have a slight negative bias in ice drafts compared to the ULS data (−0.06 m overall), with standard deviations ranging between 0.54 and 0.72 m (0.60 m overall). These errors include the differences between the satellite swath versus ULS point measurements, time that the satellite was actually over the location versus averaging period, as well as variations in the seasonal signals discussed previously. The relationships from the satellite data are reasonable for thinner ice where the surface properties are able to discern young and older ice, but are less certain for thicker ice. To reduce the uncertainties in the estimates, only averaged results from IJIS drafts are used here, but better handling of melt ponds and fine tuning the ratio relationships could generate a more refined product with better accuracy.

Providing information in all seasons, the spatial variations of these ice draft estimates compare qualitatively with altimeter-based satellite ice thickness products. The IJIS product deviations are only slightly greater than the deviations reported for the IceSat-derived product (0.51 m; *Kwok et al*. [2009]) and twice the Cryosat-based product (0.24 m; *Laxon et al*. [2013]) when compared to the same BGOS ULS data (but over different time periods). Comparison of 10 day averages of 10 day IJIS means from the 10 day ULS means at the same location (not shown) indicates an overall positive offset of 0.10 m and standard deviation of 0.42 m. The relationship between the sonar measurements and radiometer measurements are utilized for

estimating the solid component of fresh water over most of our temporal range, including the summer months. While thin ice categories (young ice and first-year ice) may be discerned from multiyear ice using established satellite radiometer data methods, the relationships between observed thickness and satellite radiometer ratios for thicker ice are more dependent on ponding and seasonality and less well constrained. However, the 10 day IJIS product results are sufficiently statistically sensitive to variability that the areal means can be utilized with reasonable precision for first-order budgeting of freshwater content.

4.3. Sea Ice Categories

Distinguishing between ice types (e.g., first-year and multiyear ice) based on thickness alone can be misleading because mechanical processes such as ridging and rafting can produce ice thicknesses in nearly all categories. Furthermore, as thicker ice types melt away they must pass through the thinner categories. Consequently, here we avoid characterizing our results based on ice types, but instead categorize according to ice thicknesses. However, following *Hansen et al*. [2013], we select thickness categories based on World Meteorological Organization sea ice nomenclature [*World Meteorological Organization*, 1970] to allow comparison with other published results.

To estimate ice thickness from the draft measurements, ice drafts are scaled by a fixed ratio of ocean to ice densities (which are assumed to be constants). From the JOIS summer hydrographic data [*McLaughlin et al*., 2010; *Williams*, 2010] and year-round Ice-Tethered Profiler (ITP) data [*Toole et al*., 2011; *Krishfield et al*., 2008] in the BG, mixed layer density is estimated to average 1022 kg m^{-3} since 2003, and the density of ice is estimated at 910 kg/m^3 [*Timco and Frederking*, 1996], so that the scaling factor equals 1.123. Consequently, the following ice thickness designations are utilized in this paper: *Category 0* includes all ice thicknesses less than 0.3 m (ice drafts less than 0.3 m including zero) which typically contains open water and young ice; *category 1* includes ice thicknesses between 0.3 m and 2 m (ice drafts between 0.3 m and 1.8 m) typically associated with first-year ice but also may contain ablated multiyear ice; *category 2* includes ice thicknesses between 2 m and 3 m (ice drafts between 1.8 m and 2.7 m) typically containing multiyear and old ice; and *category 3* includes ice thicknesses greater than 3 m (ice drafts greater than 2.7 m) typically containing ridged ice.

4.4. Fresh Water Calculations

Fresh water calculations of the liquid component in seawater are referenced to a salinity of 34.8 following *Proshutinsky et al*. [2009] (see *Carmack et al*. [2008] for discussion of reference salinities). Errors for the fresh water calculations for individual profiles are estimated to be less than 0.1 m, and after optimal interpolation the uncertainty varies between 0.5 and 1.25 m (or between 500 and 1250 km^3 when converted to fresh water volume in the BG), depending on year.

The solid fresh water component locked in the sea ice (neglecting snow cover) are determined from the measured ice draft, the estimated seawater density (1022 kg m^{-3} as above), and estimated bulk salinity of the sea ice. From Archimedes principle, the mass of the frozen sea ice is equivalent to the mass of the seawater displaced by the ice, which must also be equivalent to the mass of melted ice water of the sea ice in liquid form so that:

$$\rho_i \cdot h_i = \rho_{sw} \cdot h = \rho_{iw} \cdot h_{iw} \quad (1)$$

where ρ_i = density of sea ice, h_i = thickness of sea ice, ρ_{sw} = density of displaced seawater, h = ice draft (displaced thickness), ρ_{iw} = density of melted ice water, and h_{iw} = thickness of melted ice water layer. The density of the melted ice water is determined at the freezing point using a specified bulk salinity of sea ice (s_i in ppt, which is also by definition the salinity of the melted sea water) and the fresh water in the melted ice water layer is integrated over the thickness of the layer, also referenced to salinity = 34.8 so that:

$$h_{fwi} = (\rho_{sw}/\rho_{iw}) \cdot (1 - s_i/34.8) \cdot h \quad (2)$$

where h_{fwi} is the fresh water content in the sea ice (referenced to 34.8) per unit area.

Uncertainty in the seawater density of a few kg m^{-3} introduces an uncertainty less than 1%, as does neglecting the snow cover. On the other hand, varying the bulk sea ice salinity from 1.8 to 2 ppt reduces

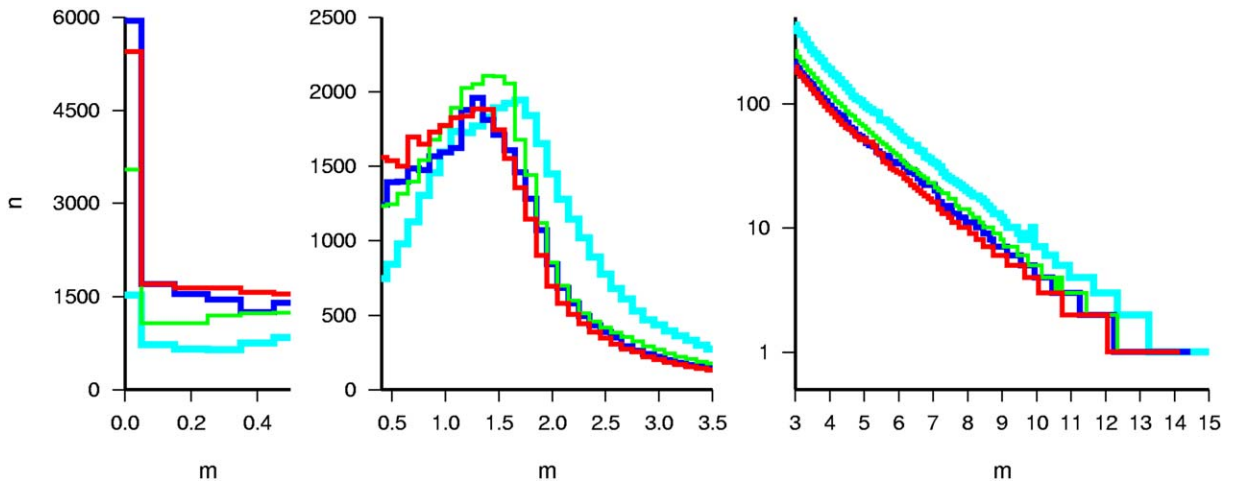

Figure 4. Mean ice draft histograms (by number of 2 s observations per day) in 10 cm bins using all data from each BGOS mooring location (A red, B green, C cyan, and D blue) separated into three panels by thickness. Note that the record from mooring B contains gaps from 2005 to 2006 and 2009 to 2010 during the 9 year time period, C data are only available from 2003 to 2008, and D data are only available for 2006–2012. The histograms are separated into three panels with different *y* axis ranges and scaling (logarithmic scale is used on the right) to magnify differences according to the different ice thickness ranges.

the fresh water calculation by only 0.5%, but to 3 ppt by another 3%, and to 5 ppt by another 6%, so that the selection of salinity can be significant to the calculations. While young ice and first-year ice tend to have higher salinities during formation, brine drainage throughout winter reduces the salinity so that old ice and ridged ice tend to have salinities on the lower end of the scale. This is reflected in the curves of bulk salinity variation versus ice thickness for first-year ice up to 2 m thick and old ice between 2 and 9 m thick produced by *Kovacs* [1996]. In this study, we are primarily concerned with solid fresh water in the summer season, after brine rejection and during melting so expect salinities in the lower ranges of the curves. This means that salinities in ice less than 2 m are presumably between 4 and 5 ppt, and in thicker ice are between 1.8 and 2 ppt. Consequently, a bulk sea ice salinity of 3 ppt was chosen in equation (2), so as to bracket the uncertainty in the fresh water estimates in either direction by 3–4%. Our final conversion is then:

$$h_{fwi} = 0.932 \cdot h \tag{3}$$

5. Sonar Ice Draft Results

In this section, time series of ULS derived ice draft at each mooring site are presented using histograms of the temporal distributions (or frequency) of observations binned in increments of 0.1 m for the entire record, and later for multiyear time periods. The daily histograms for each mooring for all years are combined according to day of year and scaled by the total number of observations to produce contour plots of the fraction (in percent) of ice drafts in 0.1 m bins throughout the seasonal cycle. Ten-day running means of the time series and defined ice categories at each mooring location are presented for the duration of the data set to analyze the interannual variability. Monthly averages of the annual cycles at each mooring location are removed from the detrended time series to resolve anomalies and determine trends. Finally, spatial distributions are calculated at each mooring for a portion of the time series using an independent ice motion data set and compared to the temporal distributions. The observations show that the overall thickness of the ice pack in the BG peaked in 2006 and has been deteriorating since, leaving the region exposed for the significant summer ice reductions in 2007 and 2008, and complete loss in summer of 2012.

5.1. Mean Distributions

To examine the overall character of the data set, we first present histograms of ice draft for each mooring throughout the record (separated into three panels by thickness in Figure 4), and contours of the daily distributions throughout the annual cycle superimposed with computed daily mean and median time series (Figure 5). Together these plots indicate that there is strong similarity in overall ice draft distribution at each station and in their seasonal cycles, but that there are also significant differences.

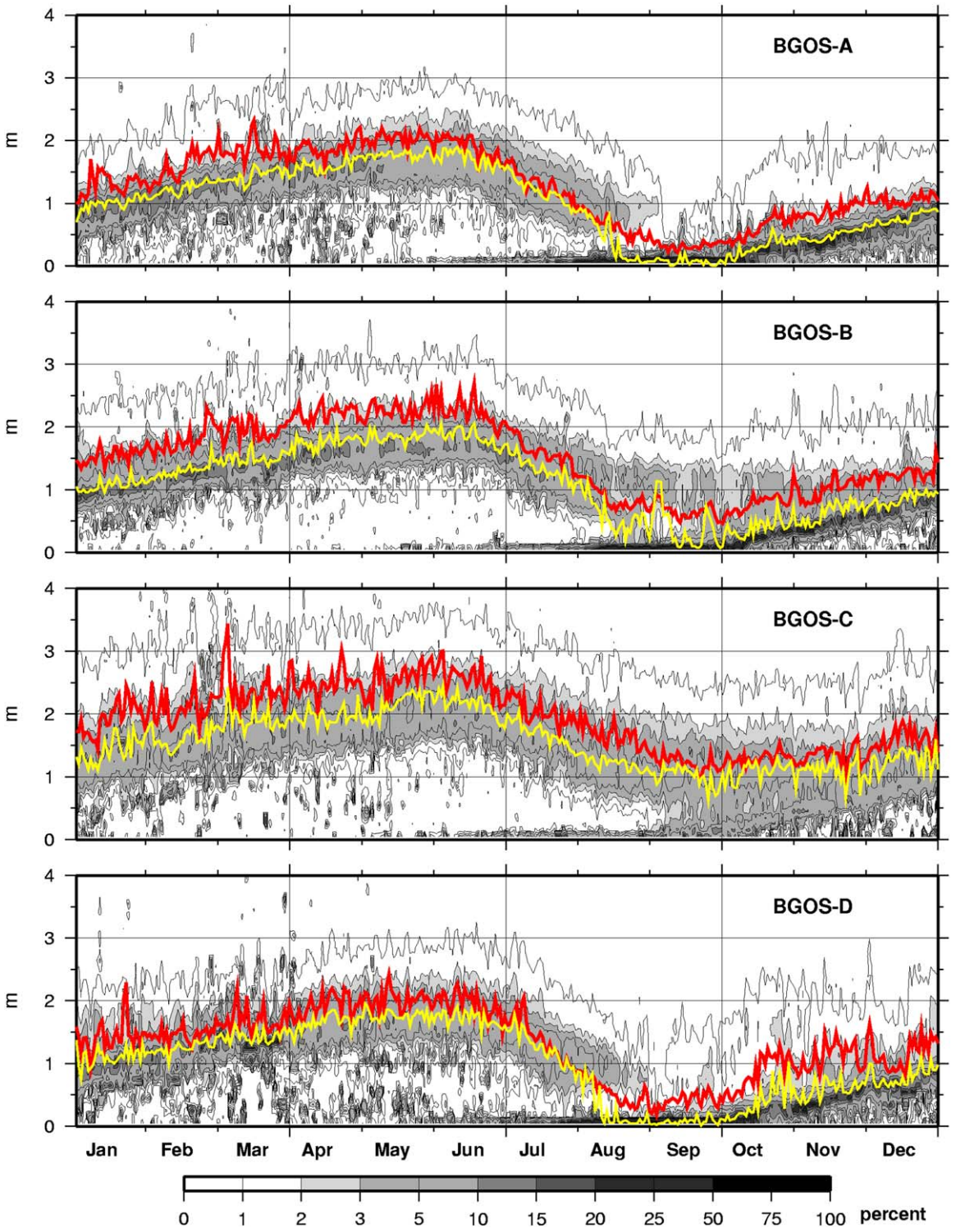

Figure 5. Contours of the daily distributions of ice draft throughout the annual cycle from all years (in percent occurrence) superimposed with computed daily mean (red line) and median (yellow line) time series for each BGOS mooring location.

It is notable that none of the histograms from any of the moorings have a local maximum greater than 2 m which would indicate the presence of a *category 2* (>2 year old) ice mode which was found in the Beaufort region of the Canada Basin in previous decades (see Figure 5 in *Wadhams and Horne* [1980]), instead a mode is centered between 1.3 and 1.8 m *category 1* ice. Not surprisingly, the two northern stations in the

perennially ice covered region (B and C) have 1.5–2 times greater amounts of thicker ice (>3m) and 0.25–0.5 lesser amounts of thin ice (<1m) and open water than the seasonally ice covered southern stations (A and D). The mode of ice draft at mooring location C is greater than the modes at the other locations, but this could be biased by the fact that data from C are only available for the first 5 out of the 9 year time period being considered.

5.2. Annual Cycle

The annual cycle of daily distributions of ice draft at each mooring location throughout the 9 year period are plotted in Figure 5 as shaded contours delineating the percentage of occurrences per day within 5 cm bins. The computed daily mean and median time series are also plotted on the same panels, whereas the modes over the course of the year can be inferred where the percentages are maximal (darkest shades). All of the plots indicate similar seasonal cycles with ice draft minima in late summer slowly and steadily increasing to maxima in late spring, with a sharper more rapid decline back to the minima during summer. At the southern stations (A and D), the 1% contours are generally below 3 m around the seasonal maxima, but generally slightly above 3 m at the northern stations (B and C). Due to the characteristic skewness of the distributions (e.g., Figure 4), the time series of the means typically exceed the medians, and the medians typically exceed the primary ice modes. Secondary thin ice modes become evident beginning in October at all of the moorings, but are least pronounced at C. The increasing thickness of these modes over time primarily indicates the thermodynamic growth rate of first year ice as it develops, although ice thickness also increases during mechanical ridging processes as well. Summer means exceeding 1 m in the data from mooring C resembles a perennial ice time series, whereas the data from the other moorings better resemble a seasonal ice time series. The record from mooring C, however, is only 5 years long.

5.3. Interannual Variability

Time series of ice draft and ice type fraction measured at each mooring are presented as plots of 10 day running-means (Figure 6). The mean ice draft (across all mooring sites) peaked in the winter of 2005, and then decreased steadily afterwards with approximately 0.5 m decline over the 9 year period (∼0.05 m/year). Concurrently, open water fraction was minimal in 2005, and maximal in 2008 and 2012. Three distinct time periods stand out in the time series: (1) before summer 2006; (2) after summer 2008; (3) and the period in between. Before summer 2006, the mean ice drafts from the northern stations (B and C) are significantly (0.5 to 1 m) greater than at the southern station (A). After summer 2006, the differences are much reduced, except from summer 2007 to 2008 when the means from the southern stations (A and D) often exceed the northern stations (B and C). These same patterns emerge in the time series of the ice types. In particular, the *category 2* and *category 3* ice components mirror the distinctions between the northern and southern stations.

Overall, a decline in the mean ice draft and fractions of *category 2* and *category 3* ice is observed, and an increase in *category 0* is apparent. There is also an increase in the *category 1 ice* component. Most of the decline occurs in 2007 and 2008. The 2010 data are distinguished by an abrupt increase in *category 2* and *category 3* ice before summer, but are biased to only two mooring sites as the instrument at mooring B malfunctioned that year. Although the sudden increase in thicker ice types corresponds to a sudden decrease in the *category 1* ice in late winter, it is unlikely that rapid growth could create that much thick ice so rapidly. Ridging and rafting would reduce the ice area, but the fraction of *category 0* was less in summer 2010 than previous years. Consequently, this *category 2* and *category 3* ice had to have been advected from the region north of the Canadian archipelago into the BG (as indicated by ITP buoy vectors).

Also note the large spike in the *category 2* and *category 3* ice fraction time series recorded by mooring A that occurred in March 2012 in Figure 6, and which may have contributed to open water at all mooring sites for the first time at the end of the time series in August 2012. In the months prior to the extreme minimum in 2012, significant pulses of older and thicker ice in the ice draft time series passed over the mooring sites, suggesting the removal of the thickest categories of sea ice from the region. Also of note are the double peaks of ice drafts around 1 and 2 m at mooring D, and similar peaks of slightly lesser magnitude at mooring A.

The long-term changes of sea ice characteristics at the different sites are clarified by histograms of ice draft determined on a multiyearly basis for each mooring (Figure 7). The plots on the left show that the

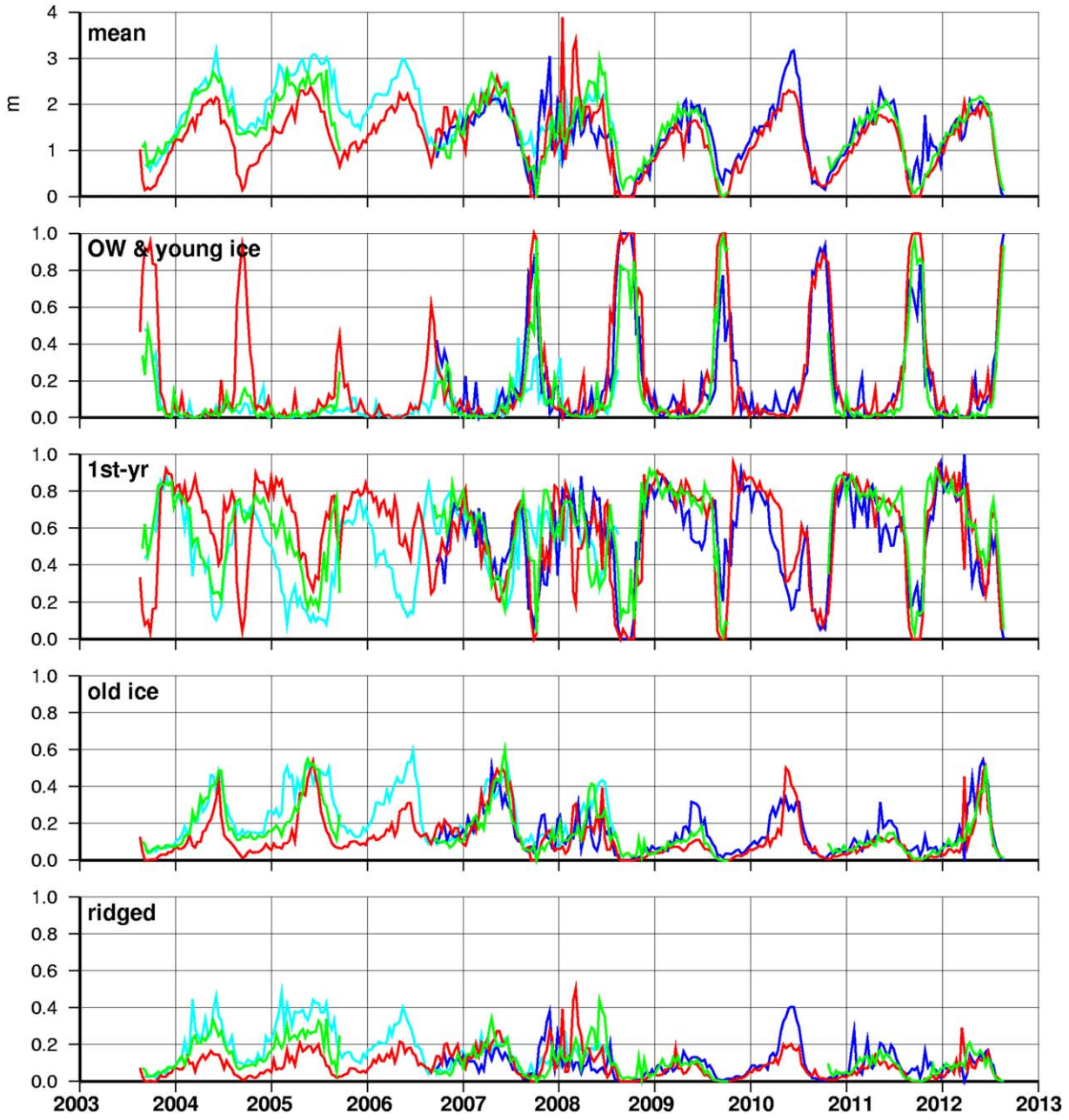

Figure 6. Ten-day running mean time series of ice draft, and fractions of *category 0*, *category 1*, *category 2*, and *category 3* ice for all BGOS mooring locations (A red, B green, C cyan, and D blue). Ice categories are defined in section 4.3.

distribution of *category 0* has increased between each of the summer-to-summer time periods: 2003–2006, 2006–2008, and 2008–2011 and January to August 2012. Middle and right plots show that the distribution of *category 2* and *category 3* ice drafts has decreased from 2003 to 2012. Only at BGOS-A do the thinner ice fractions reduce and thicker ice fractions increase from the first to the middle years (2006–2008), while BGOS-B remains the same, and at BGOS-C the thinner ice fractions increase and thicker ones decrease, opposite to A. Subsequently, the thinner ice increases and thicker ice decreases at all observed sites from the middle to the later years. The greatest reduction occurs between the 1.5 and 3 m ice draft categories on all moorings, whereas the fraction of all ice draft categories less than 0.5 m increases from the first to the last years of the time series. The panels for mooring D also includes a trace for mean ice draft distributions from unpublished data with unknown accuracy obtained by moored ULS from 1990 to 1997 located just

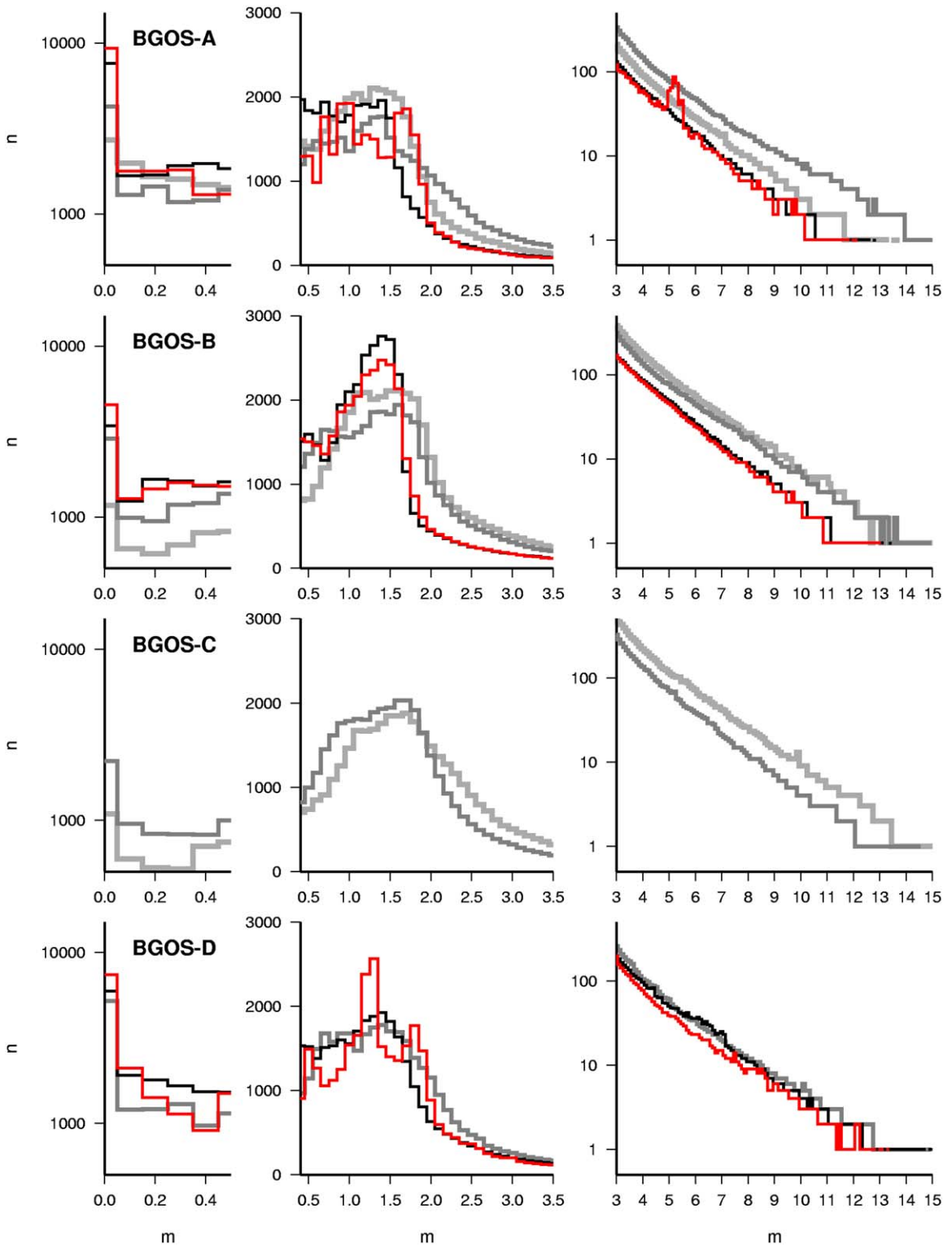

Figure 7. Histograms of ice drafts (by number of 2 s observations per day) in 10 cm bins for each BGOS mooring location in multiyear summer-to-summer time periods (mid 2003–2006 light grey, 2006–2008 medium grey, 2008–2011 black, and January–August of 2012 red). On the mooring D plots, the blue dashed line denotes *Moritz* [1992] ice draft results from the 1990s and just south of D (adjusted to compensate for the different sampling interval). Note that logarithmic scaling of the number axes are used on the rightmost plots.

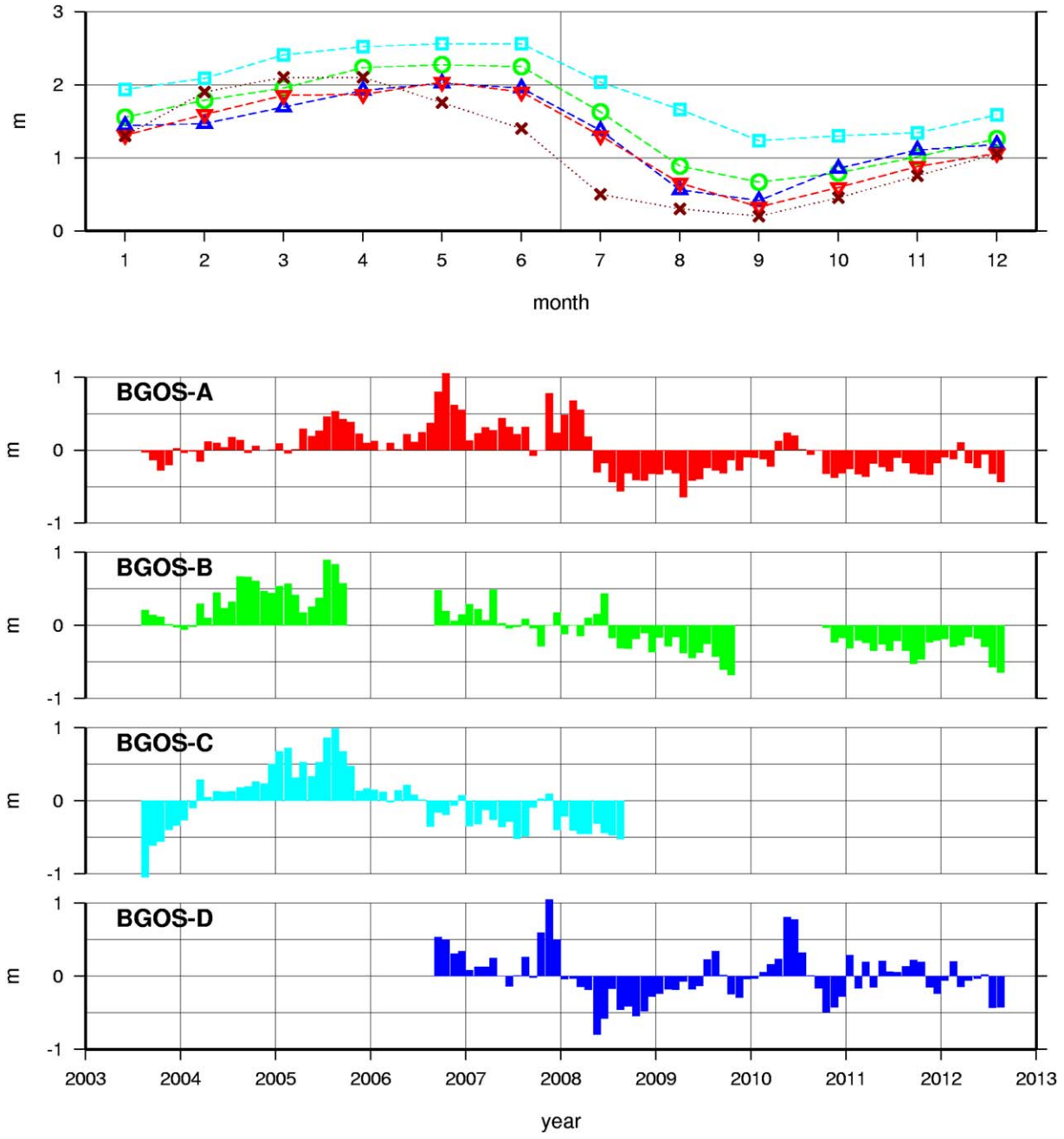

Figure 8. (top) Annual cycles of decadal mean ice drafts computed from all data for each BGOS mooring (A red, B green, C cyan, and D blue) used for computing anomalies. For comparison, the brown dotted line is the annual cycle from a 12 year time series ending in 2003 for a mooring located on the southeast Beaufort Shelf [*Melling et al.*, 2005]. (bottom) Monthly anomalies of ice draft with the annual cycle removed for each BGOS mooring location.

south of the present location of D [*Moritz*, 1992]. The mode of ice draft in the 1990s is slightly greater than in the 2000s, and the fraction of thin ice categories is less, attesting to a more substantial ice pack in this corner of the BG in the previous decade.

5.4. Monthly Anomalies and Trends

The length of the time series and regularity of the seasonal cycle (Figure 5) allows interannual variability to be viewed in terms of monthly ice draft anomalies once monthly means for each mooring have been removed from each detrended time series (Figure 8). The first 3 years (summer 2003 to summer 2006) of the record are dominated by increasing positive anomalies of ice draft at all moorings (A, B, and C). Between

Table 2. Table of Time Series Trends With 95% Confidence Limits From Monthly Mean Ice Draft Anomalies[a]

Mooring	Neff	Mean	Category 0 (<0.3 m)	Category 1 (0.3–1.8 m)	Category 2 (1.8–2.7 m)	Category 3 (>2.7 m)
A	55	−0.53 ± 0.66	18.6 ± 30.1	−4.7 ± 34.5	−8.3 ± 16.1	−5.6 ± 10.2
B	44	−0.95 ± 0.61	18.2 ± 36.0	−3.1 ± 41.4	−9.2 ± 19.2	−5.8 ± 12.5
C	31	−0.85 ± 1.18	11.9 ± 45.7	−36.5 ± 46.9	9.0 ± 20.4	15.5 ± 12.9
D	36	−0.33 ± 0.66	24.8 ± 25.6	15.1 ± 30.6	−20.9 ± 14.8	−19.0 ± 8.9

[a]Mean ice draft trends are given in m/decade, Neff is the effective degrees of freedom based on a 2 month decorrelation time, and ice category trends are given in percent/decade. Data gaps exist in the mooring B record during the third and seventh years of the 9 year time period, mooring C data are only available for the first 5 years, and mooring D data are only available for the last 6 years.

summer 2006 and summer 2007, moorings A and D saw significant positive ice drafts anomalies but small (at B) and negative draft anomalies (at C) farther north. The positive anomalies at site D continue until the end of 2007, and at site A until spring 2008. The large positive and subsequent negative anomalies between winter 2007 and winter 2008 indicate a 4 month lag between mooring D and A consistent with a westward surface circulation of 3–4 cm/s in the southern portion of the BG. Even this relatively short 9 year time series is able to discern a sharp change from positive to more consistently negative ice draft anomalies between fall 2007 and spring 2008. Afterwards, the negative ice draft anomalies at all sites decreased until the exceptional summer of 2012.

Calculated ice draft trends from the monthly anomaly time series quantify the ice reduction in Table 2. The confidence limits were calculated based on the effective degrees of freedom determined after estimating decorrelation time scales. The effective degrees of freedom varied between 31 and 55 over the four moorings so that the confidence limits are wide. The trend at mooring A suggests an overall loss of over 45 cm of ice thickness over the 9 year period, while at mooring B the implied loss is more than 80 cm. The implied loss at mooring C (for the first 5 years) is 40 cm, and at mooring D (for the last 6 years) is only 18 cm. The trend in category 0 fraction at all moorings implies an increase of 17–22% over the 9 year period. There are negative trends in the *category 1* ice fraction at all the mooring locations except D. On the other hand, all mooring locations except C show negative trends in the *category 2* and *category 3* ice components, most significantly at D. Overall, this suggests a redistribution of ice from the thicker to thinner (or ice free) categories, consistent with ablation.

5.5. Spatial Distributions

To determine whether irregular ice drift speeds influence temporal draft statistics at each mooring site, spatial distributions at the individual sites are estimated from the ice draft time series using concurrent ice velocity data to map to regular spatial increments [e.g., *Melling et al*., 1995]. While both expressions representations characterize the amount of ice over the length of the time series, the conversion to length scale adjusts the sampling based on drift speed so that the ice draft measurements are weighted by distance covered. Without ice velocity measurements on the moorings, a pan-Arctic daily 25 km gridded ice motion data set derived from satellite and drifting buoy data from 2003 through 2012 [*Fowler and Tschudi*, 2003, updated 2012] was used. Although the coarse temporal and spatial resolution of the ice motion data set is not ideal, it does have the advantage of covering all areas in all seasons.

If the BG circulated at a constant velocity in a contained area and the ice was distributed uniformly, then ice draft distributions either temporally or spatially would be the same at each mooring site. Spatial histograms (in 0.2 m bins for this plot only) estimated both from our mooring and the gridded ice motion data set are plotted (Figure 9) and, although differences vary somewhat, they are not large. For both, peaks are evident at 0 m and about 1.5 m corresponding to open water and *category 1* ice, respectively. It appears that the temporal distributions may slightly underestimate the amount of ice less than 1 m thick and slightly overestimate the amount of ice between 1 and 2 m thick. When the data are compared on an annual basis for each mooring (not shown), these differences are enhanced before summer of 2005 and after summer 2010, and largely insignificant in between. Overall, the agreement suggests that the ice is rather uniform in the region, and the drift largely regular. Therefore, we do not expect irregularities in the temporal statistics as might be the case, for example, if ice movement stopped or slowed while a thick floe was over the ULS, as can be the case in shallow waters and near shorelines.

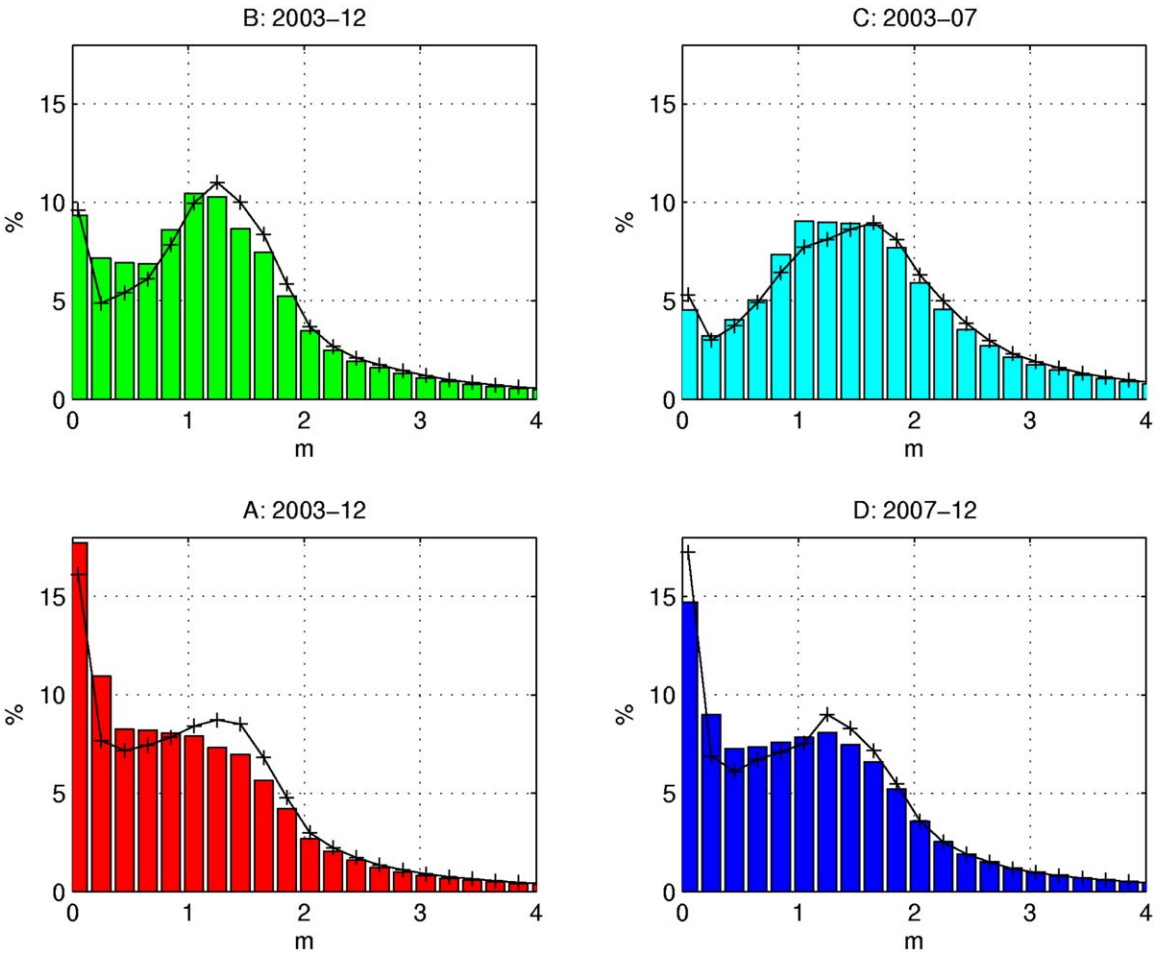

Figure 9. Histograms of ice drafts (in 0.2 m bins) for each mooring site calculated using ice motion data to convert time scale to length scale, over plotted with ULS time series distributions (black lines).

6. Areal Ice Draft Estimates

IJIS 10 day average ice drafts estimates for summer of 2003 through winter of 2011 are created to summarize the spatial distribution of ice conditions in the BG at the extremes of the annual cycle for each year (Figure 10). Both the ULS ice draft data (Figure 6) and the IJIS estimates suggest that sea ice was thickening or accumulating in the BG until winter 2006. Consistent with the positive anomalies in Figure 8 at the moorings, the thickest mean winter ice draft seasons occurred during the winters before 2007, with overall regional averages exceeding 2.3 m, and the thickest ice observed in the southern half of the BG in 2006. The IJIS mean ice draft in winter is lowest in 2007, then increases until 2009 and decreases again, all below a regional average of 2.3 m. In summers, the thickest overall ice draft mean occurs in 2005 and the thinnest is in 2008. Direct comparisons of the timing of the IJIS areal minima and maxima with the ULS point data are ambiguous due to differences between the different mooring sites and missing data. *Category 2* ice is present in summer only in the northeast of the region in several years, but *category 3* ice is not found, perhaps unresolved by the coarse gridding, or beyond the range of the ice draft algorithm. Unfortunately, the AMSR-E sensor failed before 2012.

7. Freshwater Content Components

Combined satellite and ULS measurements allow for estimates of the contribution of sea ice changes to changes in fresh water content in the BG. Fresh water stored in the ice pack in the BG is roughly estimated using the average of the 10 day running ice draft measurements for all moorings, and daily passive

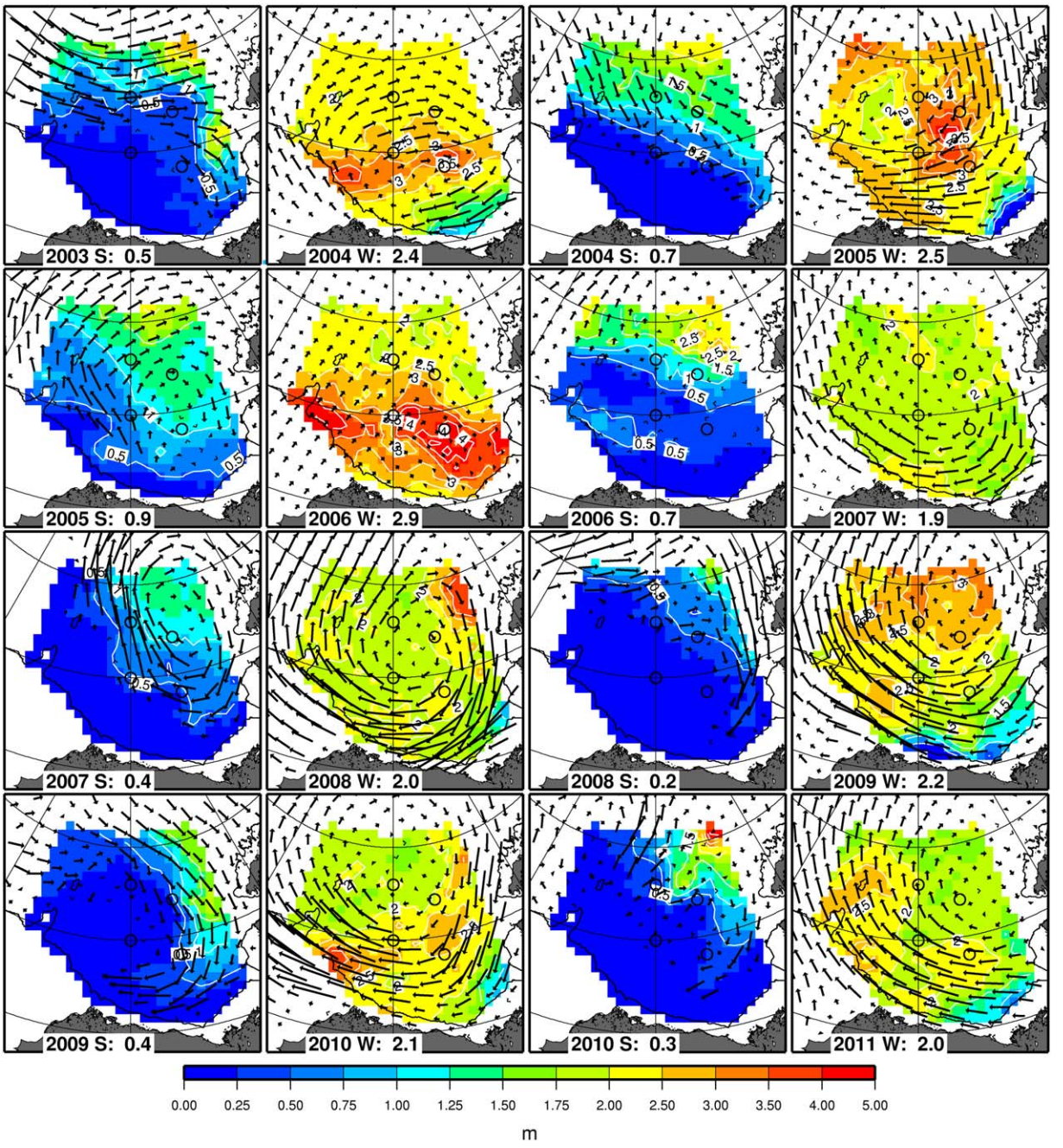

Figure 10. Contour of 10 day averages of ice draft (in m) estimates using the IJIS algorithm on AMSR-E satellite data in the BG at each summer minima and winter maxima (see Figure 11) over plotted with monthly averaged ice drift vectors. Circles mark the locations of the BGOS moorings, and the numbers at the bottom of each panel are the regional ice draft means for each period.

microwave ice concentration data from the National Snow and Ice Data Center (NSIDC). This estimation assumes that the average ice thickness from all moorings is representative of the ice pack in the BG. To test this assumption, IJIS drafts are averaged at 10 day intervals and the mean time series of the four mooring locations is plotted against the mean time series for all 49,910 grid cells in the region (Figure 11, top). The agreement between the traces is excellent, indicating that the combination of data from the four mooring locations adequately characterizes the overall conditions of the ice cover throughout entire area of the BG.

The mean ice draft at each grid cell is converted to fresh water height, which is then multiplied by the ice concentration at each grid cell. All cells are added together to calculate the solid fresh water contained in

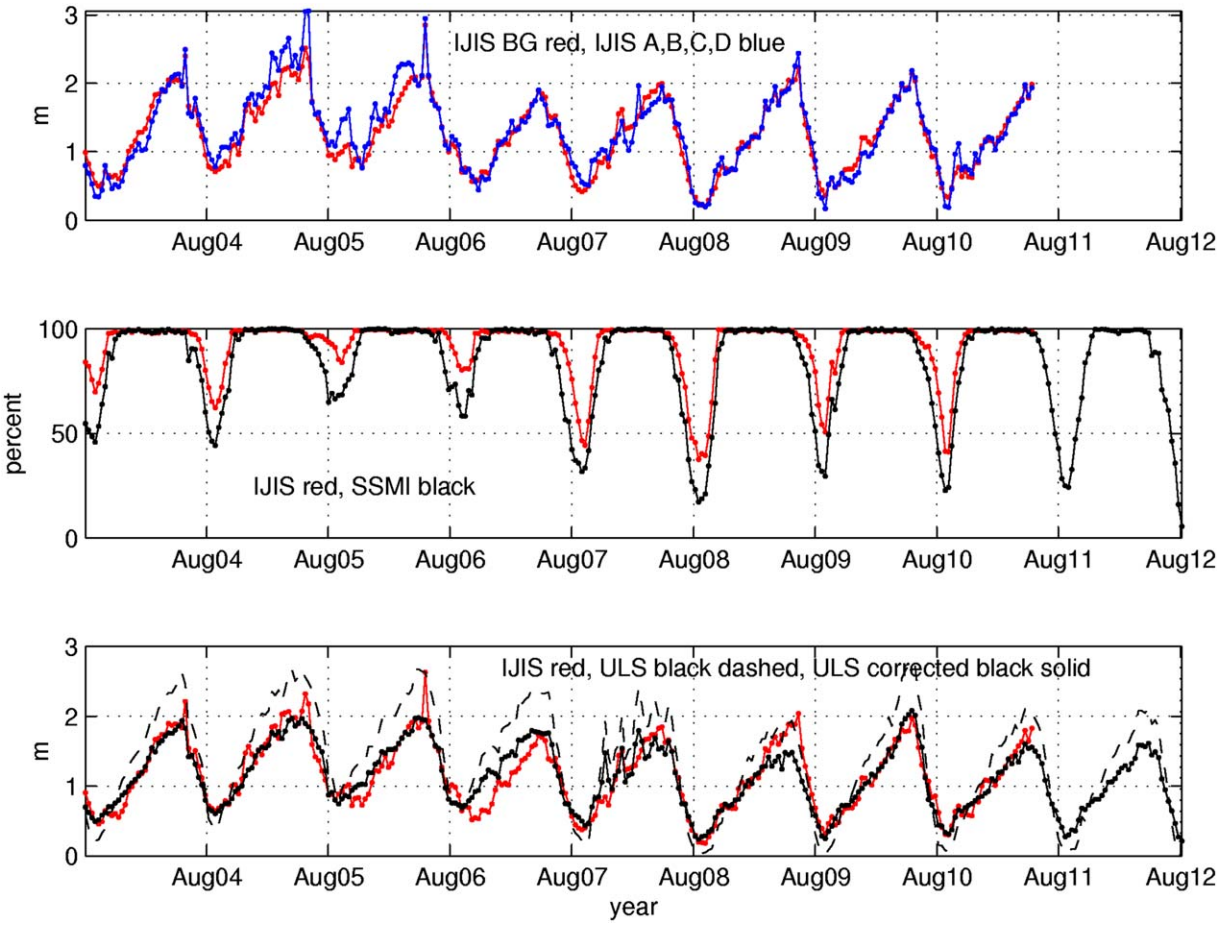

Figure 11. Plots of 10 day averages. (top) Mean IJIS ice drafts at the mooring site locations (blue), and the mean of all IJIS ice drafts in the BG (red). (middle) Mean IJIS AMSR-E (red) and Bootstrap SSMI (black) ice concentrations in BG. (bottom) Mean solid fresh water height (in m) contained in sea ice in BG from IJIS (red), at combined ULS mooring sites (dashed), and scaled ULS mooring data with SSMI ice concentrations (black).

the sea ice in the BG. A merged NSIDC data set of daily SMMR, SSMI, and AMSR-E ice concentrations produced using the Bootstrap algorithm [*Comiso*, 2000, updated 2012] is used instead of IJIS ice concentrations from AMSR-E to extend beyond 2011. The middle plot of Figure 11 compares 10 day averages of the two ice concentration data sets, and shows that including the IJIS grid cells (that incorporate melt ponds) tends to overestimate the percentage of ice in summer compared to the SSMI data.

The bottom plot of Figure 11 plots the fresh water time series from both the ULS data and IJIS data set where ice draft and concentration are computed at each grid cell, summed, and normalized by area to result in units of length. Uncertainties are associated with the error of the ULS measurement, error of the IJIS draft algorithm, and error of the ice concentration estimates totaling 0.43 m (or 440 km^3 when converted to fresh water volume in the BG). Despite the gaps in the ULS time series at different times and different mooring locations, this agreement is also reasonable, although the ULS series tends to be greater than the IJIS values in summer and less than in winter. To refine the ULS fresh water time series, regression is performed against the IJIS fresh water time series and the regression equation used as a correction factor for the ULS time series. The results indicate that between 1 and 2 m of fresh water are exchanged between the upper ocean and sea ice in the BG each year. The magnitude of this seasonal exchange is significant and must be considered when quantifying the seawater fresh water budget.

To quantify the changes in the liquid (seawater) component of the BG ice-ocean system, optimally interpolated fresh water grids were determined using primarily JOIS hydrographic stations in summer and supplemented with data from other available cruises and updated as in *Proshutinsky et al*. [2009] for 2008–2012. Figure 12 contours the liquid fresh water content grids for the 5 year periods before and after 2008. Our

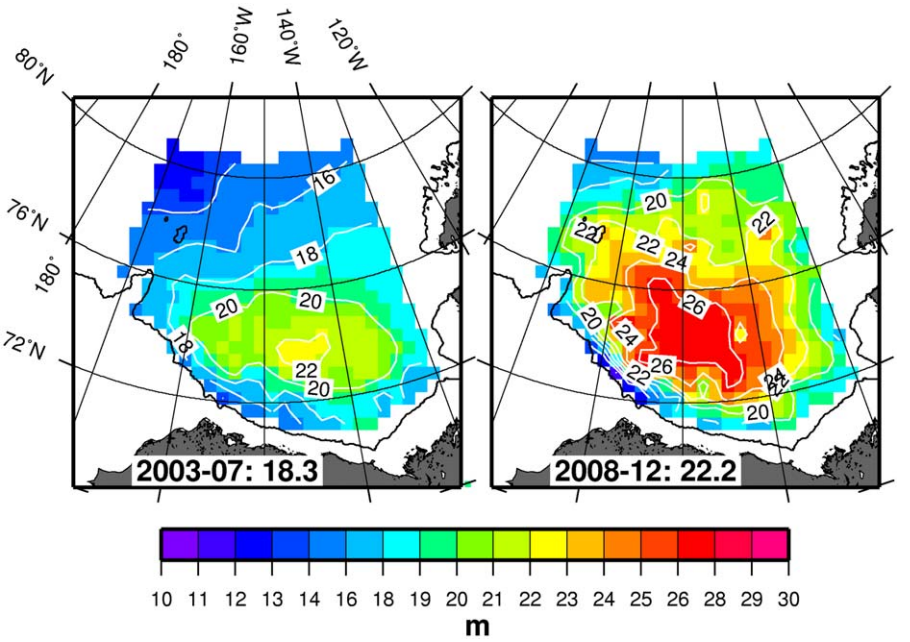

Figure 12. Contour plots of optimally interpolated liquid (seawater) fresh water (in m) in the BG from hydrographic station data from 2003 to 2007 (left) and 2008 to 2012 (right); see *Proshutinsky et al.* [2009] for further discussion of the CTD data and processing procedures. The numbers at the bottom are the volumes in 1000 km^3 averaged over the respective 5 year periods, so the difference is a 3900 km^3 (21%) gain in liquid fresh water after 2007.

best estimates of previous decadal averages based on climatological data vary between 16.5 and 17.9 thousand km^3 of fresh water content (Figure 12 of *Proshutinsky et al.* [2009]) before 2000, and only 18.3 thousand km^3 before 2008, but increase significantly since 2008 to 22.2 thousand km^3 (Figure 12).

In fact, when the solid fresh water component contained in the ice is added to liquid fresh water determined from the hydrographic station data on an annual basis (Table 3 and Figure 13 (top)), the magnitude of total fresh water in BG in summer steadily increases to 22.73 thousand km^3 in 2010 and is modestly less each year afterwards, indicating that the Ekman convergence under the anticyclonic circulation wind regime is weakening, resulting in some fresh water release from this area. Meanwhile, the summer solid contribution has decreased since attaining a maximum of 760 km^3 in 2005. Summer sold fresh water content decreased drastically in consecutive years from 730 km^3 in 2006 to 570 km^3 in 2007, and to 240 km^3 in 2008, while the ice fraction of the total fresh water dropped from 4 to 1% (Figure 13, bottom). Winter fresh water storage in ice also reduced from over 10 to 7% of the total, with most of the change due to the decrease of *category 2* and *category 3* types from as much as 90% of the winter pack before 2007 to less than 50% after. With reduced ice thickness, the annual fresh water exchange with the ocean has reduced slightly. So while the solid volume has decreased, the liquid volume has peaked and reduced slightly indicating a net export of fresh water from the region over the past several years. This fresh water release from the BG has potentially significant influence to Arctic and global climate.

Table 3. Table of Liquid (Seawater) and Solid (Sea Ice) Fresh Water Volumes (in 1000 km^3) in the BG at the Summer Minima From 2003 through 2012

Year	Water	Ice	Total
2003	17.00	0.51	17.50
2004	17.12	0.62	17.74
2005	18.47	0.76	19.23
2006	18.75	0.73	19.48
2007	19.94	0.57	20.50
2008	21.93	0.24	22.17
2009	22.00	0.25	22.25
2010	22.41	0.32	22.73
2011	22.25	0.28	22.53
2012	22.20	0.22	22.41

The solid fresh water in the ice is composed of a dynamic contribution forced by winds and ocean currents, and a thermodynamic component (i.e., ice growth or ablation due to freezing or warming). Combining the regional ice motion, ice draft, and ice concentration grids, the amount of solid fresh water as sea ice entering the BG may be determined. The net ice advected into the region is obtained by adding the contribution from all grid cells along the perimeter of the BG, using the vector component directed into the box. The area

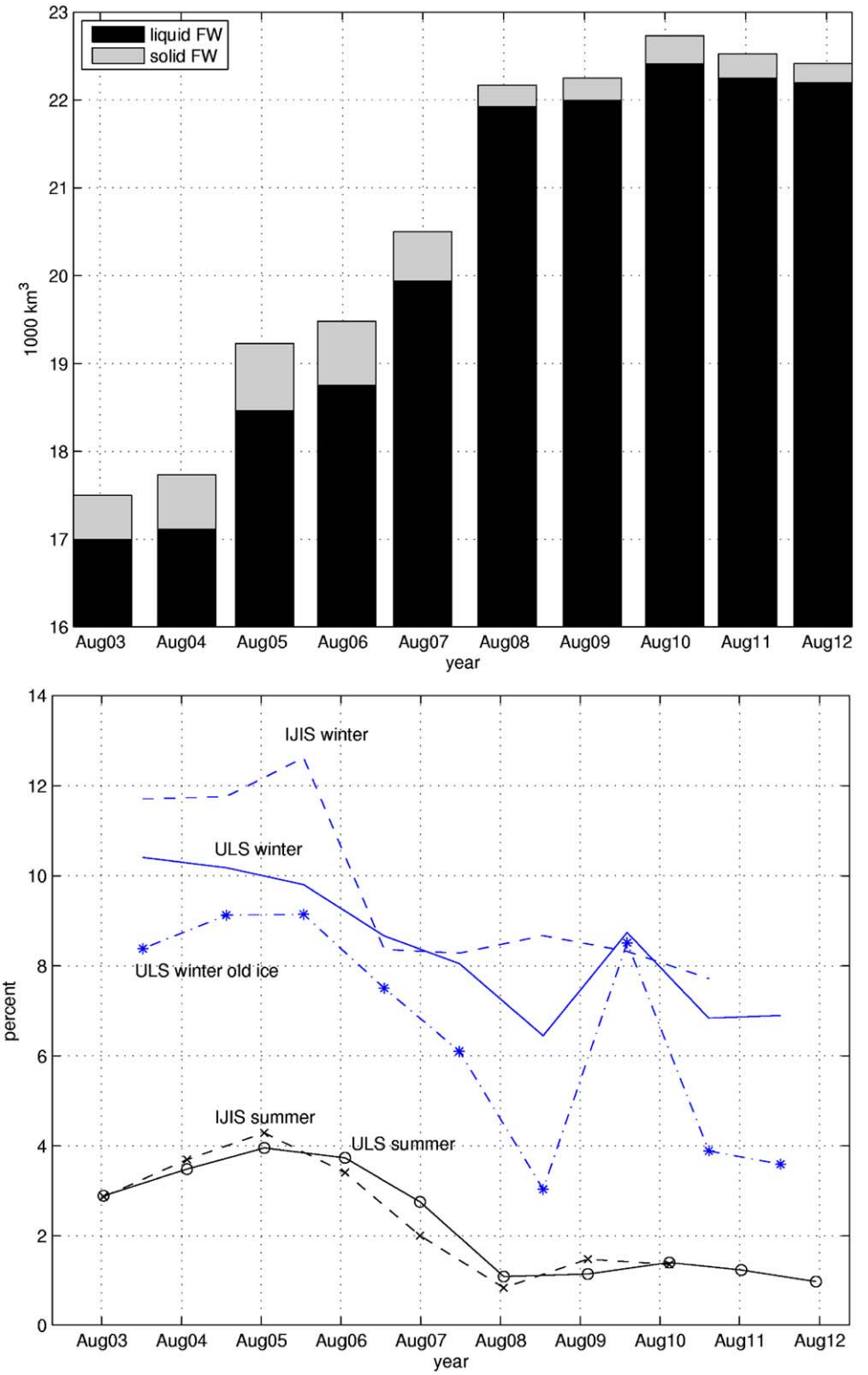

Figure 13. (top) Stacked bar plot of liquid (black) and solid (shaded) fresh water content (in 1000 km^3) in the BG at summer minima from 2003 to 2012. Note that the *y* axis begins at 16,000 km^3. (bottom) percentage of solid fresh water content from total at winter ice maxima and summer ice minima (ULS solid, IJIS dashed with symbols), and percentage of fresh water stored in *category 2* and *category 3* sea ice in winter (broken dashed).

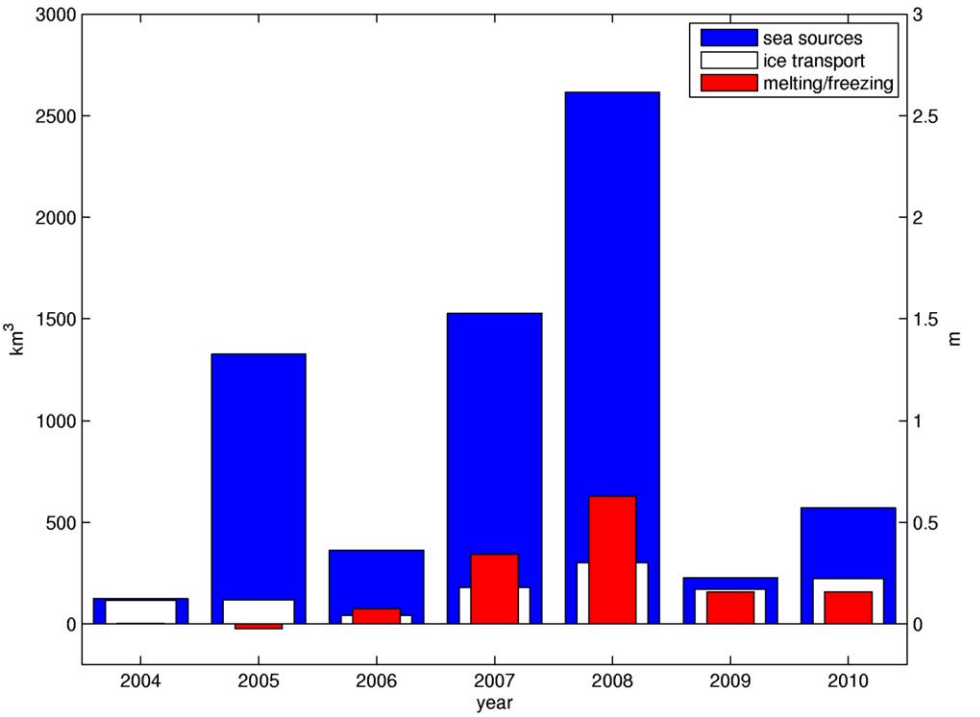

Figure 14. Change in fresh water from previous year resulting from ice advection into and out of BG (white bars), change in ice volume that melted (positive) or grew (negative) from previous year to balance the observed change in solid fresh water (red bars), and change in liquid fresh water from previous year in the BG with the contribution of sea ice melt removed from observed change in liquid fresh water (blue bars). Left scale indicates fresh water volume (in km^3), while the right scales indicate approximate fresh water content (in m).

of sea ice being transported at each grid cell is determined using the *Fowler and Tschudi* [2003, updated 2013] ice motion and IJIS ice draft and concentration grids. Due to the prevailing anticyclonic circulation patterns, there is a net positive flux of ice into the BG most months of the years, and a net increase per year. The difference between the amount of fresh water stored in ice and the net volume of ice transported into the region provides the net amount of advected ice that must have melted in place. If more ice exists in the region than advected in, then the difference must be due to net freezing. According to the present calculations, fresh water due to net ice advection into the region varied between 40 and 300 km^3 annually (Figure 14, white bars), while fresh water due to sea ice melt increased from near zero and negative values before 2006 to over 620 km^3 by 2008 and about 160 km^3 afterwards (Figure 14, red bars). These summer-to-summer values for sea ice melt volume tend to exceed the winter-to-winter estimates reported by *Kwok and Cunningham* [2010], but the variations are quite similar. The liquid fresh water in the seawater is composed of the sea ice melt component, precipitation, river runoff, and seawater of Pacific origin brought into the BG by Ekman transport. Subtracting the melt component leaves the changes in fresh water due only to the other liquid sources (Figure 14, blue bars). The right axes on Figure 14 indicate the equivalent fresh water height changes when the fresh water melt volume is divided by the area of the BG.

8. Discussion

Satellite visual, infrared, and microwave technology has allowed sea ice concentration to be observed nearly continuously and routinely since the mid-1970s, and these observations have shown that significant reduction in ice extent and area has occurred over the years, particularly in the past decade [e.g., *Comiso*, 2006; *Parkinson and Cavalieri*, 2008; *Comiso et al*., 2008; *Stroeve et al*., 2012]. Specifically, *Barber and Hanesiak* [2004] documented variability of ice concentrations in the southern BG and Amundsen Gulf region before 2005 and *Galley et al*. [2008] showed negative ice areal trends extended into the 2000s and with some correlation of these processes with the Arctic Oscillation. However, comparable sea ice thickness estimates to quantify the thinning rate and determine ice volume changes have proven more difficult to obtain.

From previous observations, 12 years of ice draft measurements over the Beaufort continental slope from 1991 to 2003 suggest only a slight thinning trend (0.07 m/decade) and high variability in the seasonal pack ice zone [*Melling et al*., 2005] leading up to the BGOS deployments. Since 2000, sonar ice draft data from submarine transects across the Beaufort Sea of ice draft have provided ice draft transects only in 2004 and 2007 [*Wadhams et al*., 2011]. In April 2007, the mean measured draft in area of the SEDNA ice camp (located at 73°N 145°W) within the BG was only 2.58 m and 43% of the ice cover was less than 2 m thick [*Wadhams et al*., 2011]. The less deformed ice was younger and thinner than the ice in 2004, offset by greater ridging.

Using ICESat altimetry, total freeboard (snow and ice) was determined by *Kwok et al*. [2007], and subsequently used to estimate a loss of ~0.6 m and 42% decrease in multiyear ice thickness was estimated from 2003 to 2008 [*Kwok et al*., 2009]. *Farrell et al*. [2009] report freeboards declined at a rate of ~1.8 cm/yr during autumn and ~1.6 cm/yr during winter over the same years. Similar methods have been developed to determine ice freeboards using radar data from ERS-1 and ERS-2 satellites [*Laxon et al*., 2003], and later CryoSat satellite [*Laxon et al*., 2013]. *Giles et al*. [2008] analyzed the ERS data and found that the mean winter thickness of sea ice in the Arctic Ocean was 0.26 m thinner after the 2007 melt season than before, and 0.49 m less in the Western Arctic (including the BG).

With greater detail, the 9 year time series of ice draft data from the BGOS bottom-tethered moorings indicate that the northern stations included significant *category 2* ice (between 2 and 3 m drafts) that persisted throughout summer prior to 2007 at the northern stations. After 2007, *category 2* ice is reduced, and most of the differences in the statistical characteristics of the ice between all of the stations are gone, indicating that the ice cover throughout the region became statistically homogenous. Negative trends in mean ice drafts, *category 2* and *category 3* (greater than 3 m) fractions are observed, leaving seasonal sea ice throughout the BG. When the 2 m annual cycle of growth and ablation is removed, computed anomalies of *category 2* and *category 3* contributions indicate a large reduction after the ice minimum in 2007. Maximum keel depths are also proportionally lower, but vary greatly. This is consistent with the observed thinner, rotten, and heavily pocketed September 2009 sea ice reported by *Barber et al*. [2009] that contained 25% more open water than the images showed. In September 2012, Arctic sea ice extent was over 650,000 km^2 (or more than 15%) less than the previous record minimum in September 2007 (see http://nsidc.org) due, predominantly, to anomalous ice reduction in the BG. The ULS results show that the big reductions of the ice pack in 2007 and 2008 had thinned the ice considerably, deteriorated, and preconditioned the region for enhanced ice reduction as suggested by *Parkinson and Comiso* [2013].

These changes in the ice cover are exchanging fresh water with the upper ocean and influencing the stratification and gyre circulation pattern, as well as providing a different biophysical environment such as nutricline depth changes [*McLaughlin and Carmack*, 2010]. Fresh water storage in the seawater component was addressed by *Carmack et al*. [2008], who discussed the southerly shift of the BG maximum in the 1990s, the components and distributions in the Canada Basin, and noted slight increases of fresh water in the BG from 2003 to 2006. *Proshutinsky et al*. [2009] discussed the role of Ekman pumping accumulating fresh water in the BG (that occurred steadily since 2003 until recently), mostly focusing on the liquid fresh water state and variability, while sea ice changes and solid fresh water content in the BG were only briefly discussed. Rather than fresh water from the ice cover, the major source of the surface fresh water has come from Russian rivers runoff [*Yamamoto-Kawai et al*., 2009; *Morison et al*., 2012]. It was assumed that sea ice conditions in the BG were relatively stable and that the input of fresh water during seasonal sea ice ablation in summer was compensated by ocean salinification due to sea ice growth in winter.

Observations presented here, however, show that under rapidly changing sea ice conditions this first-order assumption is no longer correct. Comparing the bars in Figure 14, we see that the liquid seawater components besides sea ice melt account for most of the observed changes in fresh water in all years, although sea ice melt does contribute to a significant fraction of fresh water change in some years. From summer 2003 and 2004 salinity, oxygen isotope ratios and nutrient data in the BG, *Yamamoto-Kawai et al*., [2008] found sea ice melt contributed negatively to the fresh water inventory in the BG, and was limited to the surface mixed layer. The negative contribution indicates net sea ice formation and export from the BG for those years. *Yamamoto-Kawai et al*. [2009] also analyzed salinity, oxygen isotope ratios, and alkalinity in surface waters to inventory the meteoric and sea ice melt components in the BG from 2003 to 2007, and determined that the inventory of sea ice melt turned from negative or zero in 2003–2005 to positive in 2007, particularly in the central BG where they found that the amount due to sea ice melt increased by 2.5 m. On

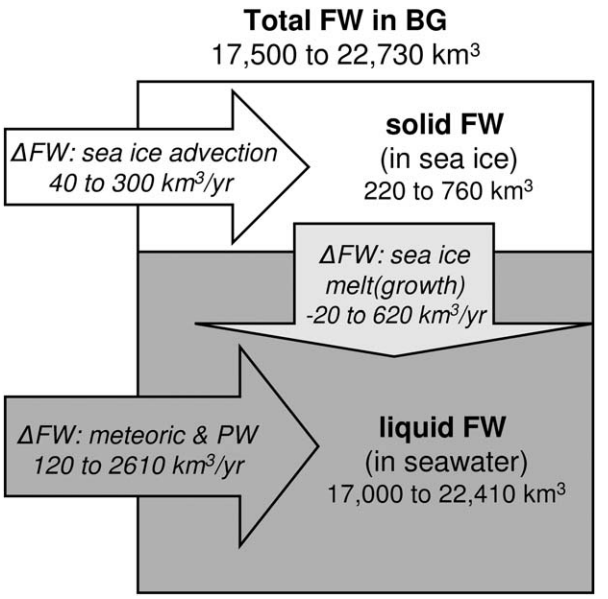

Figure 15. Schematic of solid and liquid FW components in the BG. The ranges of storage terms include years 2003 through 2012, while the ranges of flux values end in 2010.

the other hand, using summer 2003 and spring 2008 geochemical data in the upper 195 m, *Morison et al*. [2012] found a sea ice melt increase of only 0.6 m from 2003 to 2008 (adjusted for seasonal differences between the 2 years) and noted that the freshwater inventory for 2004 was similar to 2003, but their results are limited to only the southern half of the BG.

Our results (Figure 14) also show a small amount of sea ice melt (white bars) in 2004 and negative melt in 2005 (indicating net ice growth over the previous year), but melt becomes positive again in 2006 and comprises 15–18% of the liquid fresh water change each year from 2006 to 2008. An overall total of 1 m of ice ablated throughout the BG between summer of 2006 and summer of 2008. These findings agree with the results of *Perovich et al*. [2008] who attribute an increase in open water fraction in 2007 to bottom melting of sea ice in the region. Note that we observe increased open water after 2006 (Figure 6), and find that the regional ice cover in winter 2007 was much thinner than in 2006 (Figure 10). Although the amount of sea ice melt fresh water was reduced in 2009 and 2010, the amount of the other seawater fresh water components also reduced, so that sea ice melt comprised over 28% of the liquid fresh water changes in 2010 (coincidentally when the contributions of meteoric and Pacific Water sources were the least since 2004) and 16% in 2011.

The other seawater components of fresh water (Figure 14, blue bars) show large variability in their combined contribution from year to year. In 2003 and 2004 summer data, meteoric water (river runoff and precipitation) was the highest fraction of the fresh water inventory in the BG in the upper 50 m and Pacific Water was the highest fraction deeper than 50 m, and overall [*Yamamoto-Kawai et al*., 2008]. Throughout their 300 m deep water column, they estimated that the inventory of the fresh water components that they observed were being maintained by approximately equal fluxes of meteoric and Pacific Waters (0.9 and 1.1 m a^{-1}, respectively), and an annual negative contribution from ice melt (-0.6 m a^{-1}). *Yamamoto-Kawai et al*. [2009] showed that the largest component of meteoric water came from Eurasian rivers, with a smaller Mackenzie River contribution in the southern BG. This was confirmed by *Morison et al*. [2012] who also showed that the source of the largest change of liquid fresh water (in the upper 195 m) from summer 2003 to spring 2008 (again, adjusted for the seasonal difference between the two survey times) was Eurasian river runoff: 3.6 m out of the total 3.4 m increase. They attribute a -0.8 m change to the Pacific Water component, limited by their 195 m water column.

Including depths below 195 m, our calculations indicate a 6.0 m increase in seawater fresh water components other than ice melt from 2003 to 2008 throughout the BG, which accounts for most of the liquid fresh water change plotted in Figure 13, top plot. Trending similarly but more weakly, *Morison et al*. [2012] obtained only a 2.8 m increase in the southern half of the region from summer 2003 to spring 2008 (so that the contribution of summer 2008 river runoff was estimated). They indicate that the change in the Pacific Water component was small, so the bulk of the variability in Figure 14, blue bars is likely related to the meteoric water component.

Figure 14 indicates that the greatest fresh water contributions from seawater sources other than ice melt occur from 2004 to 2008, concurrent with the large reported increases in the inventory of Eurasian meteoric fresh water in the BG discussed above. However, this may be changing as we also see that the contribution

of these other seawater sources (presumably dominated by the Eurasian river runoff component) has reduced after 2008 to 2010. At the same time, the contribution of Mackenzie river water to the fresh water inventory in the BG may also be changing, as remotely sensed, optical proxy data in summer from 2002 to 2011 indicates that routing of Mackenzie water changed from primarily an eastward path into the Canadian Arctic Archipelago in 2002, to a northwestward path into the BG since 2006 [*Fichot et al*., 2013].

In summary, *category 2* ice that persisted until the summer prior to 2007 in the BG is absent afterwards, and differences throughout the region significantly diminished as the ice cover became largely uniform. Solid fresh water in the ice attained a minimum in 2008, the increase of liquid and total fresh water accumulating in the BG slowed after 2007, and the contribution of sea ice melt became more significant. Peaking in 2010, total fresh water has declined slightly since, indicating net export of fresh water from the region and that the ocean anticyclonic circulation regime has weakened. Preconditioned by the deteriorated ice conditions, the summer of 2012 saw even less ice volume in the BG than the previous minimum in 2008. Figure 15 summarizes schematically the contributions of the solid and liquid fresh water components in the BG FW budget.

Appendix A

ULS data processing procedures are described in more detail. ULS data files retrieved after each recovery of each instrument are saved in a single binary data file. Using the ASL IpsLink software and instrument specific configuration files (including calibrations), the raw files are decoded into four separate files: a BRS file for burst sampling (not being used), a PNG file containing the range data, a PRS file containing the pressure, temperature and tilt data, and a SYN file with the time clock.

Hydrographic profiles from CTD stations at the beginning and end of each year-long time series are used to correct the ULS pressure and temperature data and determine water level. NCEP SLP reanalysis data are used to remove the atmospheric load (which can vary by as much as 1 m) from the pressure readings. High-frequency fluctuations (presumably due to waves in open water conditions) are eliminated using a 20 min running mean filter on the tilt and water level.

The raw ranges decoded using the software are based on sound speeds used during instrument calibrations (normally 1450 m/s). Variations in sound speed can yield a 10–30 cm error in the measurement (depending on open water and ice conditions). Ranges are filtered and smoothed with a five point (10 s) running mean average (to eliminate wave noise and increase precision) and are adjusted for instrument tilt. Ice draft is determined from:

$$\text{Ice draft} = \text{water level} - \textit{beta} \cdot \text{range} \cdot \cos(\text{tilt}) \tag{4}$$

where water level is determined from the pressure measurements corrected for atmospheric load. The *beta* correction incorporates changes in seawater temperature and salinity (which vary the actual speed of sound over the path of the ULS pulse), and is necessary to reduce the final error of the draft measurements. A semiautomated method was utilized that combines *beta* estimates based on the observed temperature and *beta* estimates from detectable open water segments to objectively average *betas* every 3 h within 1.25 day centered windows. The method is tuned with parameters that are manually adjusted to each data set.

The data processing functions and script codes described here are written to operate in the MATLAB environment. The overall processing sequence is outlined in Figure A1. The pressure, temperature, tilt data, and battery voltage data (PRS and SYN files) are processed before the range data (PNG file).

A1. Pressure Data Processing

The processing steps for the raw pressure, temperature, and tilt data provide calibrated smoothed time series of tilt, temperature, and water level (depth from pressure and density). The major steps are: (1) correct seawater pressure for atmospheric pressure; (2) scale pressure using CTD data to produce water level; (3) correct temperature bias and trend using CTD casts; (4) smooth tilt and water level; and (5) apply other platform specific corrections.

The raw PRS data are first examined (voltages, temperature, pressure, and tilt in the *x* and *y* directions [tiltx and tilty]). Typical battery voltage decays of the alkaline packs for the BGOS deployments were from 15.5 to

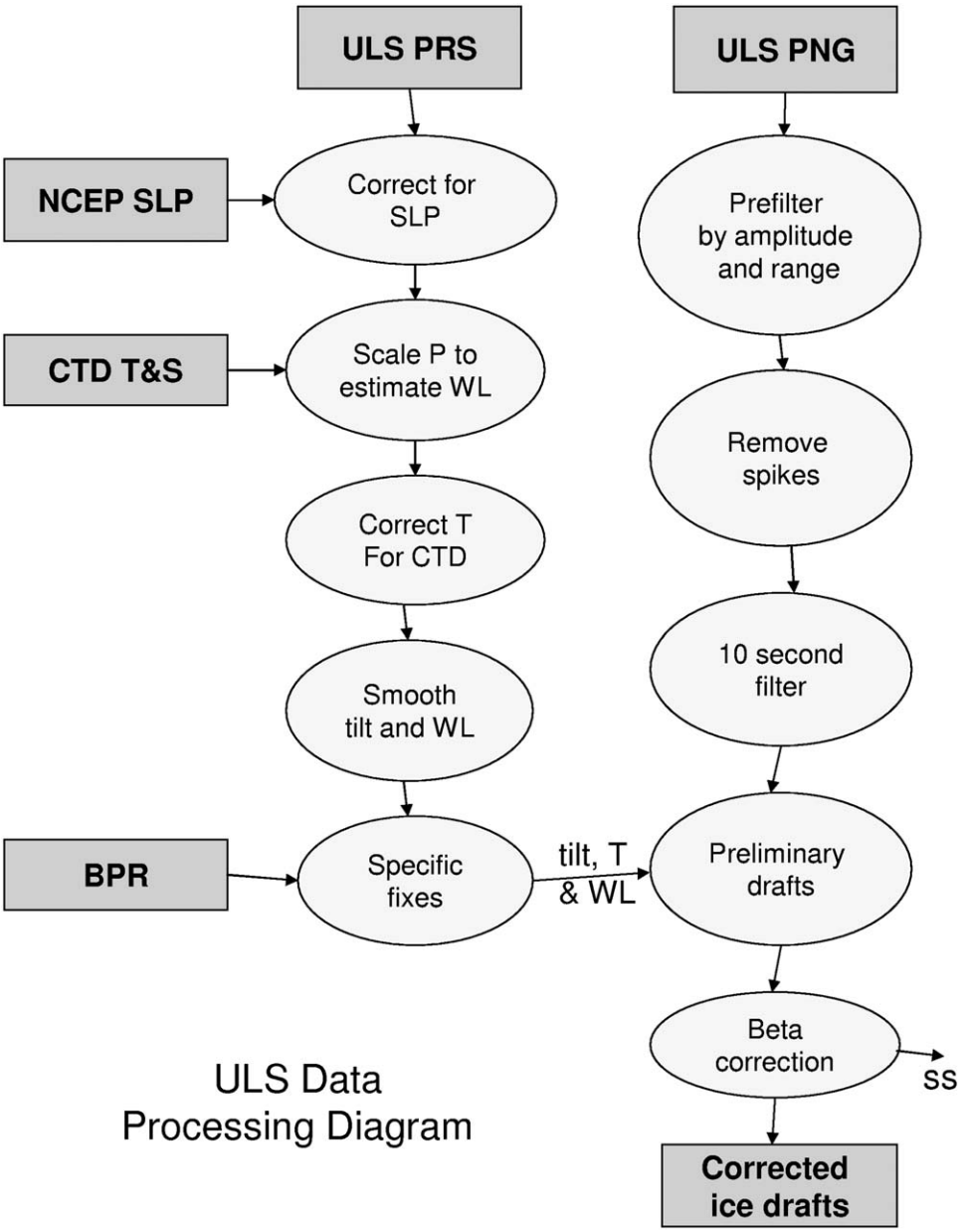

Figure A1. Block diagram showing the processing scheme used on BGOS ULS data.

12.5 V over 1 year. Negative pressure measurements are removed, as are pressures outside minimum and maximum thresholds (determined for each data set by observation). The tiltx and tilty data are combined into a single tilt magnitude. Due to the flotation holding the ULS, the magnitudes of the tilt never varied by more than a degree while sampling, even during times when subsurface eddies or enhanced currents (evident from MMP data on the moorings) dragged the surface floatation deeper (as indicated by the pressure readings). Consistently across all of the moorings, comparison with bottom pressure recorder (BPR) data from each same mooring seem to indicate that mooring wire stretch may account for about a 1 m decrease in measured pressure in a year, which shows up as a water-level variation.

The atmospheric load is equal to about 10 m in the seawater pressure measurement and varies throughout the year by ± 0.5 m. NCEP SLP are interpolated for each time and instrument location, and subtracted from the raw pressures. The mean density of the upper ocean above the ULS at the beginning and end of each deployment are averaged for determining water level (from the hydrostatic equation) and later for sound

speed calculation. The magnitude and trend of the seawater temperature at the ULS depth is also extrapolated from the annual CTD data and used to correct bias and slope of the instrument measured temperature. A 20 min running mean average is used to remove high-frequency waves from the tilt and water level time series (especially prevalent during ice free time periods) prior to the first speed of sound correction and initial draft estimates. The occurrences of these high-frequency pressure fluctuations are used during the PNG file processing to identify when waves are significantly influencing the range measurements.

The pressure data from the ULS on one mooring (BGOS-A: 2003–2004) exhibited a nonlinear behavior that needed to be removed by fitting the offset data gap to a fifth-order polynomial. The timing behavior of all ULS were found to be reasonably stable (typically drifting only 10–12 min/yr) so the only corrections to the clock were to ensure that the measurements were synchronized with UTC.

A2. Range Data Processing

The range file processing converts ranges to drafts by estimating preliminary bottom temperature ice drafts, correcting for sound speed (*beta*) variations, and returning the positive draft data. The following steps are executed: (1) prefiltering by range and amplitude; (2) spike removal and filtering; (3) preliminary draft determination; (4) sound speed (*beta*) correction; and (5) final drafts.

In the PNG files, ping amplitude is decoded along with ping range. Pings with amplitudes less than 250 are removed, as are ranges outside specified minimum and maximum thresholds. This criteria removes all the predeployment data as well as some reflected ranges (that appear shallow in the time series) that were sometimes evident in the raw data. Range spikes greater than 2 m (positives, negative, doubles, triples, and quadruples) are removed, and the ranges are filtered using a 5 point (10 s) running mean. For typical ice drift conditions ($<$10 cm/s), the averaging occurs across no more than 1 m ice, which is less than the typical footprint of the ULS.

The sound-speed correction factor is defined as *beta* = actual sound speed/instrument calibrated sound speed (usually 1450 m/s). The first *beta* correction is estimated from the instrument temperature time series. However, in the Beaufort Sea, the upper 100 m of the water column sometimes contains several temperature maximum layers that are not well represented by the temperature at instrument depth, so we expect some deviation from reality. Salinity changes are incorporated only as straight line trends between annual CTD casts. Using these preliminary "bottom temperature" *beta* sound speed estimates, preliminary draft determinations were made (with corrections for water level and tilt estimated previously). With bottom temperature correction only applied to *beta*, the estimated drafts are estimated to be accurate to only $\pm$15 cm. At times where open water is observed, *beta* can be accurately determined since the draft (=0) is known. However, difficulty occurs when the surface of the water is disturbed by waves, when long periods take place without open water leads, and when thin ice exists. While most other processing schemes rely on manual selection to discern ice openings, here we use an algorithm to objectively determine "open-water" *betas* every 3 h in 1.25 day windows.

"Open-water" *betas* are determined from the one-tenth percentile of "bottom temperature" *betas* between $-$0.1 and 0.15 m drafts. This procedure effectively chooses the near minimum sound speed which is associated with the open water (or thinnest ice). The averaging window relies on at least a few cracks or leads in the ice occurring often enough to provide opportunities to determine occasional correction points for *beta*. In instances where open water opportunities do not occur for several days, "open-water" *betas* are interpolated or extrapolated from previous *betas* in the time series. During periods where excessive variability associated from waves is evident in the pressure data, extra smoothing is performed while determining "open-water" *betas*. Periods that are dominated by waves in open water have additional processing to zero the drafts. In general, the automated procedure typically determines *betas* that are within 1–2 cm of values that would be manually selected.

Final *betas* are computed from the weighted average of two-thirds "open-water' *betas* with one-third "bottom-temperature" *betas*, thereby including both the temperature fluctuations and "open-water" corrections. The final *betas* are reapplied to the range data and corrected ice draft estimates are produced. Ice drafts less than zero are forced to zero and missing *betas* are linearly interpolated. The total error on draft values is estimated to be better than 10 cm.

Data are available on the BGOS website data section (http://www.whoi.edu/beaufortgyre) as time series of each 2 s ice draft determination, or as daily average ice draft statistics with daily average water temperature, water level, and sound speed.

Appendix B

The ice draft algorithm for AMSR-E data that is used here is adapted from an ice thickness measurement method using passive microwave radiometer Special Sensor Microwave Imager (SSM/I) data developed by *Tateyama et al*. [2002] for sea ice in the Sea of Okhotsk by comparison with in situ sea ice thickness data consisting of deformed thick ice ranging from 0.2 to 0.8 m, obtained by downward looking video observations from an ice-breaker in the southernmost part of the Sea of Okhotsk in February, 1996–1998.

Furthermore, Antarctic sea ice thickness and brightness temperatures have been recorded continuously by synchronous operation the ship-borne electromagnetic induction device (EM) and portable passive microwave radiometers mounted on the Japan Maritime Self-Defense Force auxiliary icebreaker *Shirase* since the 2006–2007 Antarctic summer as a part of Japanese Antarctic Research Expedition (JARE). In the Arctic Ocean, similar measurements have been conducted by the Canadian Coast Guard ice-breaker *Louis S. St-Laurent* since 2009 as a part of the Joint Ocean Ice Study (JOIS) scientific program and IARC-JAXA Arctic research project. The results of these studies have been to identify relationships to develop a sea ice thickness algorithm for satellite passive microwave radiometers based on the ship-based measurements.

A polarization ratio (PR) of 36 GHz is used for calculation of thin ice, and a gradient ratio (GR) between 6 GHz and 36 GHz for thicker ice, based on a threshold of the difference of the two gradient ratios. The penetration depth of 6 GHz is deeper than the other frequencies and is therefore better for providing information on thicker ice properties. A sea ice thickness estimation algorithm developed using these ratios was applied to the AMSR-E ratios and compared with daily average ULS ice draft data from 2003 to 2011. The comparison revealed significant variation through the year, and that the error fluctuated cyclically with season, presumably related to the seasonal changes of surface salinity, density, temperature, snow cover, and water content (melt ponds). As a result, the initial algorithm was modified to minimize error empirically using a simple approximation based on date according to comparison with the ULS drafts. Validation is accomplished by comparison to on ice measurements and moored ULS data.

B2. Data and Methods

The data that forms the basis of the relationships are based on observations of ice thickness determined from a hanging EM and ship-mounted portable passive microwave radiometer during summer cruises in the BG between 2009 and 2012. Relationships observed in the vertically and horizontally polarized components in radiometer data to observations are used to construct an algorithm for estimating ice draft from AMSR-E data. A gradient ratio is used to partition the ice between first-year ice and older ice categories. For the first-year ice and young ice, an equation based on PR developed on Antarctic sea ice is used to estimate ice thickness. For older ice, the gradient ratio tuned to the ice in the BG is also used to estimate the thickness. The relationships break down due to surface ponding and porous ice, so a seasonal correction is applied against the ULS ice draft observations, and a reasonable statistical approximation for the BG is obtained.

B2.1. EM In Situ Sea Ice Thickness and Concentration Measurements

Ship-borne EM measurements of sea ice thickness were made by combining an EM instrument with a laser altimeter mounted (or hanging) over the side of an icebreaker [*Tateyama et al*., 2006]. A single frequency EM sensor (EM-31/ICE, Geonics Ltd., Canada) operating at 9.8 kHz with a transmitter (Tx) and a receiver (Rx) coil separated by 3.66 m measures the distance from the sensor to the bottom of the sea ice at the ice-ocean interface. A laser altimeter (LD90–3100HS, Riegl Japan Ltd., Japan) detects the distance from the sensor to the surface of snow or ice.

The Tx generates an alternating primary magnetic field H_p and induces small eddy currents in the underlying seawater. These currents generate a secondary magnetic field H_s, which is sensed along with H_p by Rx. The EM instrument automatically transforms the measured quadrature response of H_s to the apparent conductivity σ_a in mS/m [*McNeill*, 1980]. Because the difference in the conductivity between snow and ice is very small, the EM instrument cannot distinguish snow from ice. Therefore, we consider the relationship between σ_a derived from EM measurements and the observed total thickness of snow and ice. The total thickness is calculated by subtracting the distance between the EM sensor and the snow/ice surface (Z_L) measured by a laser altimeter from the distance between the EM sensor and the seawater surface (Z_E). The σ_a value can be measured by either the horizontal coplanar (HCP) mode or the vertical coplanar (VCP)

mode of the EM instrument. We chose the latter mode for EM measurements, as it has a finer lateral resolution than the HCP mode and possesses a high capability of distinguishing thin ice [*Reid et al*., 2003]. According to *Reid and Vrbancich* [2004], the footprint size for the VCP geometry is 1.4–1.5 times larger than the Z_E; i.e., when sounding a 6 m thick ice ridge at an instrument height of 4 m ($Z_E = 10$ m), the apparent footprint size for the VCP mode is 14–15 m. Therefore, the instrument should be placed at least 5.6–6.0 m away from the ship's hull for the VCP mode at an operating height of 4 m, so that the ship does not influence the observed data.

B2.2. Microwave Sea Ice Measurements

Observations of microwave radiation from sea ice were conducted using a portable passive microwave radiometer system developed by Mitsubishi Electric Tokki Systems Co., Ltd., Japan, which also developed the satellite microwave radiometer AMSR/AMSR-E. Three microwave/milliwave radiometer system are used for three frequencies: 6, 18, and 36 GHz with both vertical and horizontal polarizations except 18 GHz (abbreviated 6 GHz-V, 6 GHz-H, 18 GHz-V, 36 GHz-V, and 36 GHz-H). A radiation thermometer and a visible camera provide microwave brightness temperatures and surface temperature in Kelvin, and its visible image.

The observational accuracies of the portable microwave radiometers and the radiation thermometer are within 1 K and 10%, respectively. The observation and validation time of the microwave radiometers are every 0.1 s, and the measured brightness temperatures are recorded in 1 s integrated intervals. The instantaneous field of views of the microwave radiometers and the radiation thermometer are from 7.0 degree at 36 GHz to 33.0 degree at 6 GHz and 2.7 degree and the spatial resolutions at 20 m distance are 2.5 and 0.9 m, respectively.

The portable microwave radiometers were mounted on the ship about 10 m aft of the EM at a 55° incidence angle to the sea surface, which is same angle as the AMSR/AMSR-E/AMSR2, to develop a sea ice thickness estimation algorithm using those satellite sensors.

B3. Relationship between EM Thickness and Microwave Data

Using Antarctic EM data, the thickness of thin ice is related to a microwave PR, presumably due to the relationship of brine reduction with growing sea ice. A microwave GR is used to discern between the first-year ice and multiyear ice, and is related to the thickness of older ice obtained from EM measurements in the BG.

B3.1. Polarization Ratio

The observed brightness temperatures by the satellite sensors mix the signal between open water and ice, or thinner ice and thick ice. Although differentiation between them using a single frequency and polarization channel is impossible, the physical parameters which can be derived from the multichannels of brightness temperatures are valid.

Cavalieri [1994] proposed the ratio of the brightness of polarization channels at 19 GHz (PR_{19}) based on several observational studies as a sea ice classification parameter in the NASA team thin ice algorithm for seasonal ice covered areas. Specifically, the PR_{19} is defined as an equation of the brightness temperatures (TB) obtained from horizontal (TB_{19H}) and vertical (TB_{19V}) polarization channels of 19 GHz measured by SMMR and SSM/I according to the following equation:

$$PR_{19} = [TB_{19V} - TB_{19H}]/[TB_{19V} + TB_{19H}] \quad (5)$$

PR_{19} values reflect the difference between vertical and horizontal polarizations of the same frequency and are mainly sensitive to ice surface temperature and salinity characteristics which vary with growth in the seasonally covered areas. When ice is formed, a highly saline liquid film develops on formed ice by brine expulsion causing a decrease of microwave brightness temperature. PR_{19} values decrease from young ice to thick, snow-covered first-year ice, as depolarization is related to the accumulation of snow on ice. Hence PR_{19} has been used for qualitative sea ice thickness classification for thinner ice in the Sea of Okhotsk [*Martin et al*., 1998; *Kimura and Wakatsuchi*, 1999]. *Tateyama et al*. [2002] suggested that the collective accuracy of estimation of ice thickness by PR_{19} appears to be fine, whereas the confusion between thinner ice and thicker ice still remains.

Later, *Martin et al*. [2004] proposed a new algorithm which quantifies thickness for thin ice (<0.2m) estimated from R_{37} which is the ratio of horizontal (TB_{37H}) and vertical (TB_{37V}) polarization channels of SSM/I 37

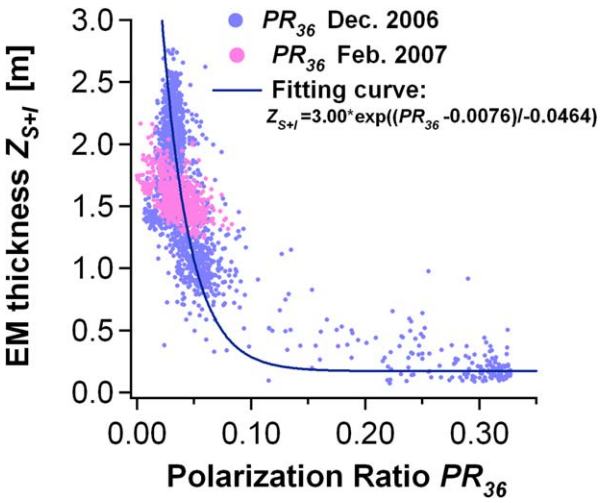

Figure B1. The relationship between EM thickness and PR_{36} derived from observation in the Lützow-Holm Bay, East Antarctica (67–69°S and 38–40°E) in 2006–2007 Antarctic summer. The blue and pink dots mean the period of December 2006 and February 2007, respectively. The solid curve means regression curve from equation (3).

GHz, in comparison with ice thickness estimated from the Advanced Very High Resolution Radiometer (AVHRR) data. *Tamura et al*. [2007] examined PR_{85} and PR_{37}, which are polarization ratios of 85 and 37GHz of SSM/I, respectively. These *PRs* were validated by AVHRR thickness in the same manner as *Martin et al*. [2004].

For the present application, we examine the sea ice thickness detecting ability of a parameter PR_{36}, calculated from 36 GHz brightness temperatures measured by ship mounted microwave radiometers on the Japanese icebreaker *Shirase* in the Antarctic. PR_{36} is calculated using the following equation:

$$PR_{36} = [TB_{36V} - TB_{36H}]/[TB_{36V} + TB_{36H}] \quad (6)$$

where TB_{36V} and TB_{36H} are brightness temperatures of vertical and horizontal polarization of 36 GHz measured from microwave radiometers, respectively.

Figure B1 shows the relationship between EM thickness and PR_{36} observed in the Lützow-Holm Bay, East Antarctica (67–69°S and 38–40°E) on the way to the Syowa station during 16–23 December 2006 (blue dots) and on the return between 10 and 14 February 2007 (pink dots), extending from early summer melt to fall freezeup. Only data for 100% of ice concentration is plotted. Sea ice consisted of four subgroups such as loose sea ice area, packed sea ice area and dry surface land-fast ice during December 2006 and flooded/refrozen surface land-fast ice during February 2007. EM thickness indicated thicknesses 0.3–1.2 m for loose ice zone, from 0.7 to 1.7 m for pack ice zone and from 1.1 m to 2.3 m for fast ice zone. Over 2.5 m thick hummock ice was observed in the edge of land-fast ice boundary. According to *Uto et al*. [2006], there is significant interannual variability of the snow and sea ice thickness, which primarily reflects the pattern of breakup of the land-fast ice in this region, ranging from about 0.8 m to 3.1 m during the past two decades. In this region, snow depth and ice thickness gradually decrease toward the shore because strong northeasterly wind cause snow drift and redistribution within a distance of 20–30 km from the shore.

A negative correlation between PR_{36} and EM thickness is shown by Figure B1. The penetration depth of 37 GHz for new ice is quite shallow, about 2 mm, due to large dielectric loss affected by brine inclusion, which is liquid saline. The TB_{36V} and TB_{36H} increase and PR_{36} decreases with brine reduction which is related to ice growth in seasonal ice. Based on the salinity and thickness relationship, PR_{36} can also be related with EM thickness.

The total thickness of snow and ice Z_{S+I} sensed by the EM is calculated by the following equation:

$$Z_{S+I} = 3.00 \cdot \exp((PR_{36} - 0.0076)/(-0.0464)) \quad (7)$$

B3.2. Gradient Ratio

In the Arctic, sea ice thickness estimation using the EM and microwave radiometers occurred during JOIS cruises in the BG. Three frequencies 6, 18, and 36 GHz, and both vertical and horizontal polarizations except 18 GHz (6 GHz-V, 6 GHz-H, 18 GHz-V, 36 GHz-V, and 36 GHz-H) were measured and synchronized with the EM. Figure B2a shows the distribution of sea ice concentration and thickness derived from AMSR-E and EM during 29 September 2010–12 October 2010. The background color map and color bars show sea ice concentration from 0% (blue) to 100% (white) and EM thickness, respectively. The southern west area was covered by thin second-year ice. The northeast area was covered by thick multiyear ice.

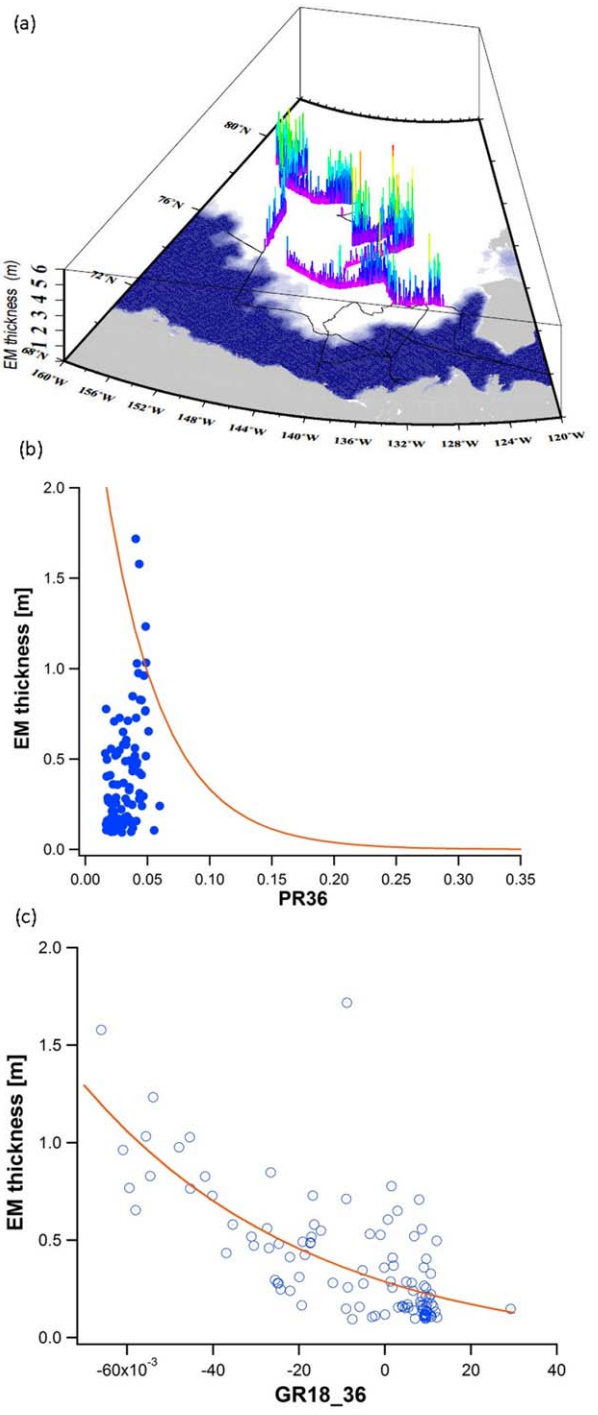

Figure B2. (a) Distribution of sea ice concentration and thickness derived from AMSR-E and EM between 29 September and 12 October 2010; (b) Relationship between EM thickness and PR_{36}; (c) Relationship between EM thickness and GR_{18-36}.

Figure B2b shows a relationship between EM thickness and PR_{36}. PR_{36} exhibits a good sensitivity for the seasonal ice whose surface salinity changes with age as aforementioned. By contrast, PR_{36} showed no relation to thickness of second-year and multiyear ice which has a fresh ice layer on the surface or deeper layer formed through summer melting season. This result suggests PR_{36} cannot be used for detecting salinity change with age or thickness because the surface layer of old sea ice has a constant low salinity.

Cavalieri et al. [1984] introduced the Gradient Ratio (GR) between vertically polarized 19 and 37 GHz GR_{19-37} as a good parameter for differentiation between first-year ice and multiyear ice in the NASA team standard ice algorithm for the Arctic Ocean. Multiyear ice is characterized by greater microwave penetration depth than first-year ice because its properties include much lower salinity and less moisture [*Ulaby et al.*, 1982]. Though the physical theory on microwave signal variations with multiyear ice thickness is still uncertain, decreasing of GR values may be attributed to volume scattering by deep snow on thicker ice [*Cavalieri*, 1994]. In this study, GR between vertically polarized 18 and 36 GHz (GR_{19-37}) was defined by the following equation and compared with EM thickness.

$$GR_{18-36} = [TB_{36V} - TB_{18V}]/[TB_{36V} + TB_{18V}] \quad (8)$$

Figure B2c shows a relationship between EM thickness and GR_{18-36}. GR_{18-36} showed a better sensitivity for the multiyear ice. This result suggested that GR_{18-36} changes with differences ice temperatures at each penetration depths of 18 and 36 GHz, and snow depth over the sea ice.

B4. Comparison Between ULS Draft and Satellite Passive Microwave Data

PR_{36} *and* GR_{18-36} were calculated from AMSR-E descending brightness temperatures and accuracies examined by comparison to daily-averaged ice draft data derived from the ULS mounted on the BGOS mooring. Although AMSR-E PR_{36} and GR_{18-36} showed agreement with ULS draft in September, GR_{18-36} thickness showed saturation and significant underestimation in other months. This suggested 18 GHz is not sensible for thickness changes; as a result GR_{18-36} reflects a sensitivity of 36 GHz for thickness of old ice. Thus a more sensitive parameter is needed for improving this method.

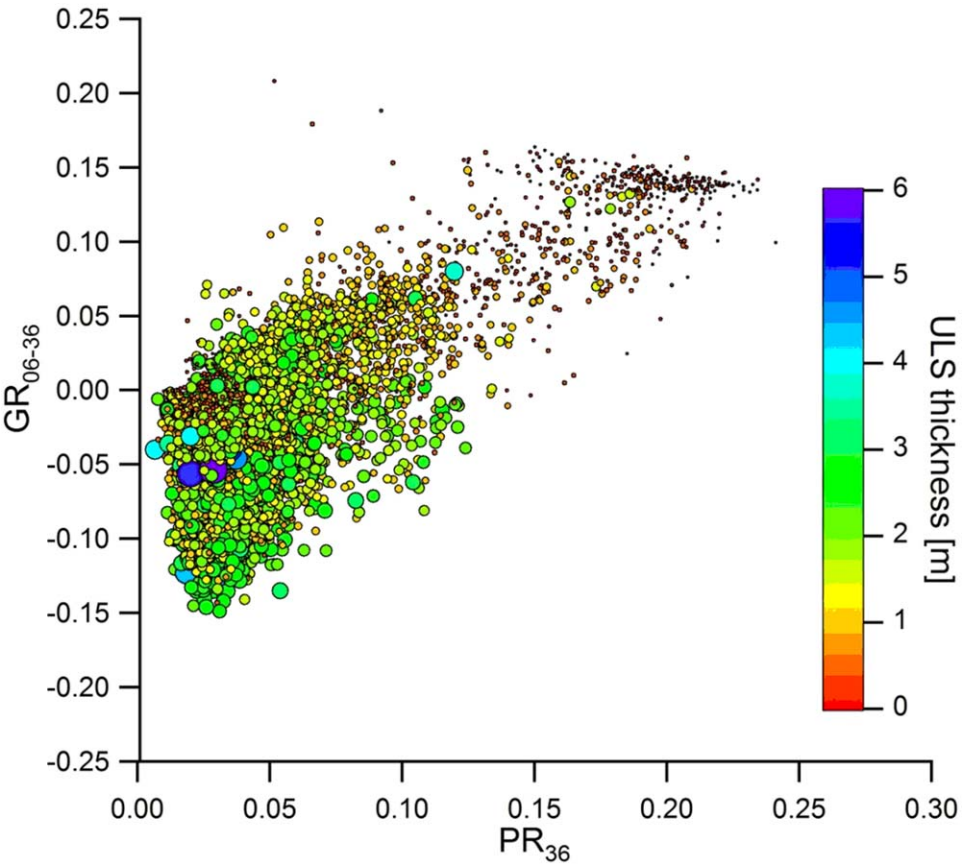

Figure B3. Scatter plot of ULS draft in the PR_{36} and GR_{06-37} space.

Relationships between ULS draft (green bar) and brightness temperatures for 6, 18, 36, and 89 GHz derived from AMSR-E display high scattering, but several characteristics were found in each frequency and polarization: 6 GHz and 36 GHz increases with ULS draft, 18 GHz is poor sensitive to ULS draft, and 89 GHz also decreases with ULS draft but scattering is large. Consequently, the difference between 6 and 36 GHz is the largest, so the most sensitive to ULS draft.

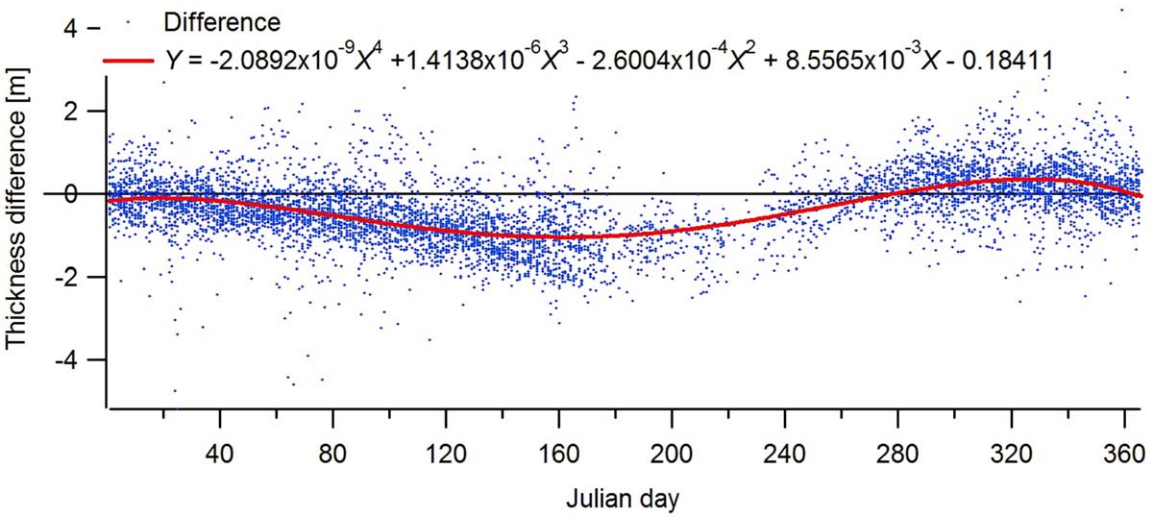

Figure B4. Seasonal change of thickness difference between IJIS draft and ULS draft.

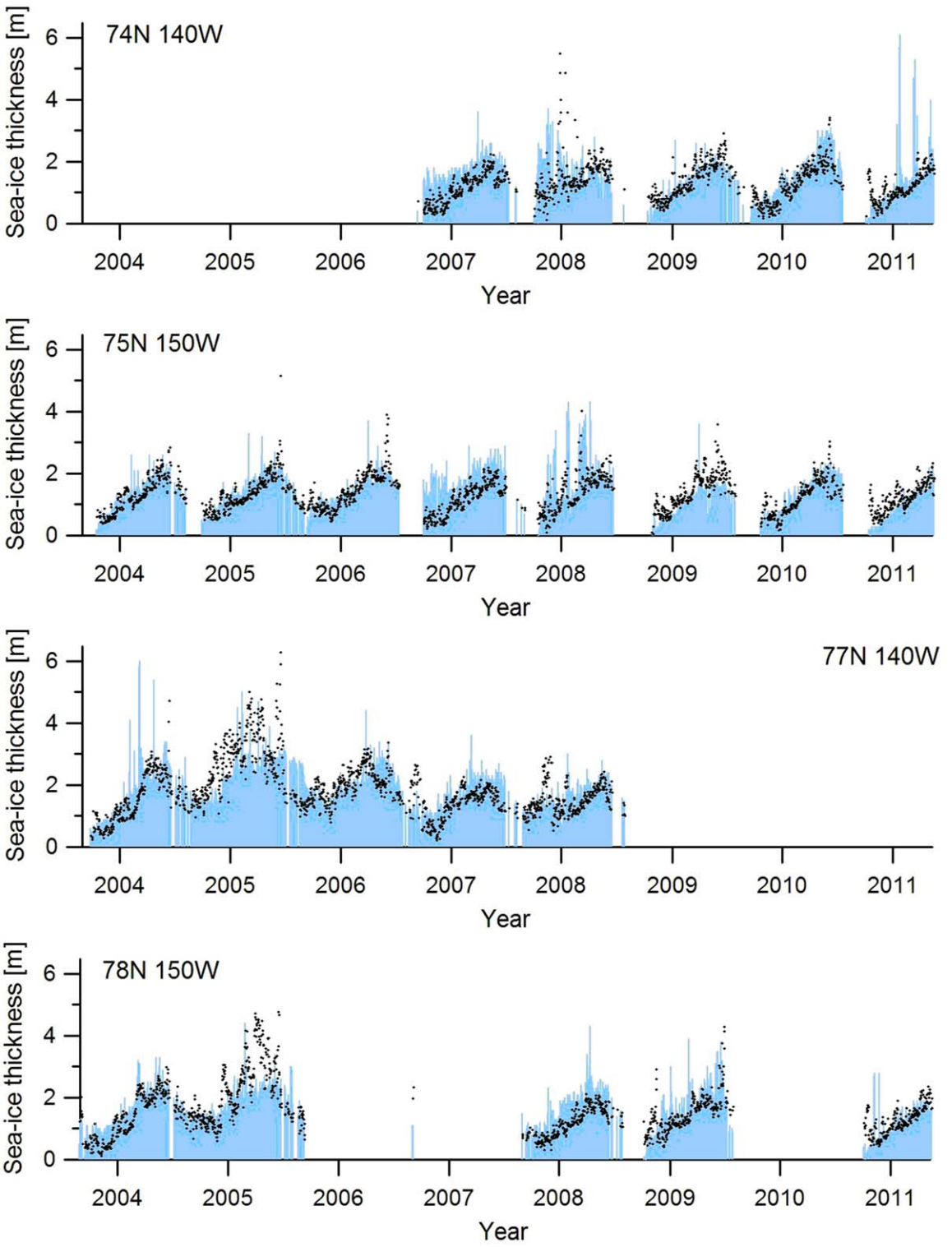

Figure B5. Time series of ULS draft (light blue bar) and modified IJIS draft (black dot).

Next, all combination of *PR*s and *GR*s for all frequencies and polarization were tested. As a result, PR_{36} was confirmed as the best sea ice thickness parameter for the first-year ice. For older ice, GR between vertically polarized 6 and 36GHz (GR_{06-37}) was most sensitive. Figure B3 shows sea ice thickness classification using PR_{36} and GR_{06-37}. Even if there is some mixture between thinner and thicker ice, smaller values of PR_{36}

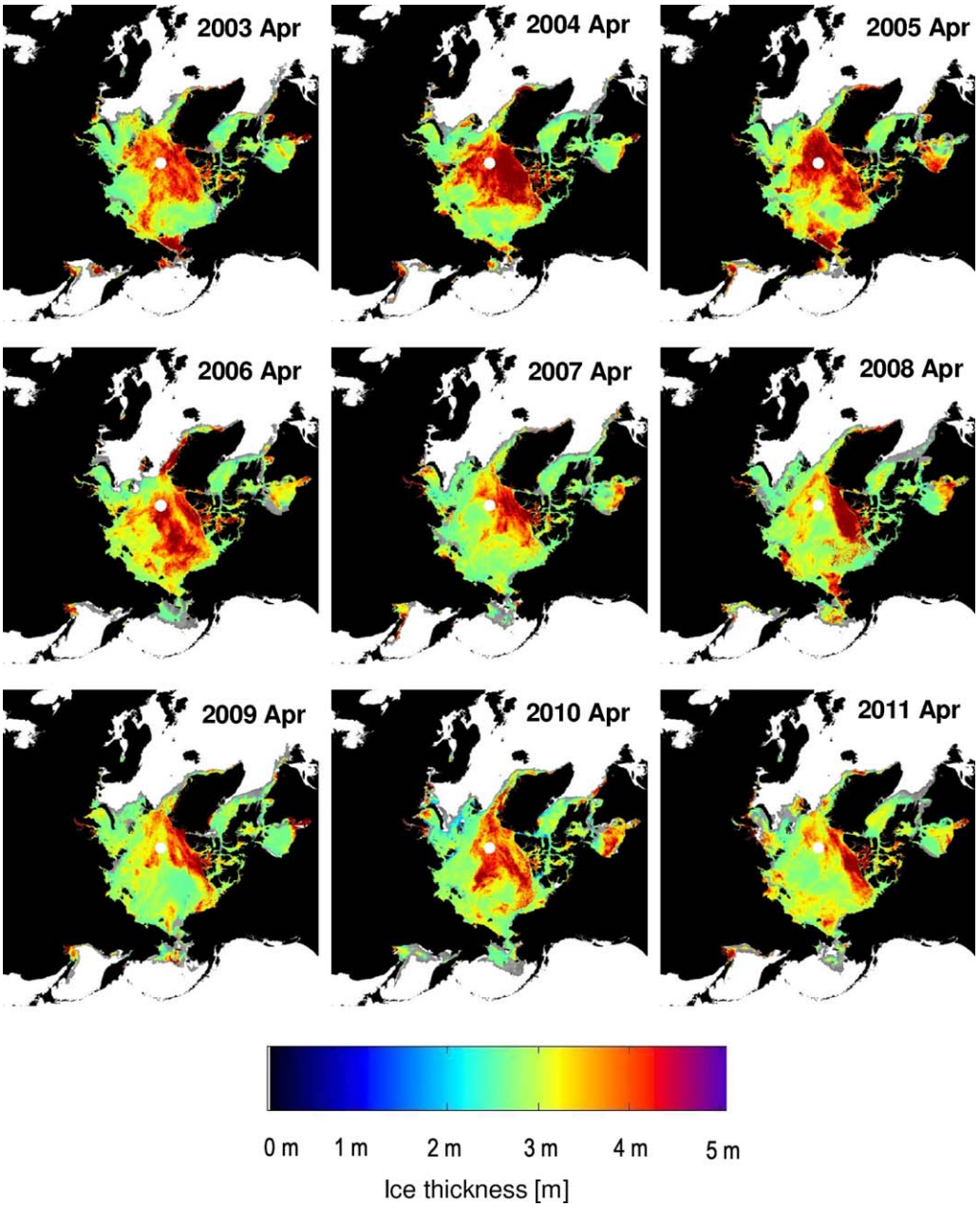

Figure B6. Examples of IJIS draft distributions for 30 April for each year from 2002 to 2011 calculated from AMSR-E data.

GR_{06-37} correspond to thicker ice. From this figure, a threshold between first-year ice and older ice was defined as $GR_{06-37} = -0.025$.

Finally, sea ice draft estimated from IJIS AMSR-E data (IJIS draft, m) is calculated from following equations:

If $GR_{06-37} \geq -0.025$, then first-year ice

$$\text{IJIS draft} = 2.34 \cdot \exp\left((PR_{36} - 0.0019)/(-0.083) + 0.085\right) \quad (9)$$

If $GR_{06-37} < -0.025$, then older ice

$$\text{IJIS draft} = 0.162 + 0.244 \cdot \exp\left(-20.79 \cdot GR_{06-37}\right) \quad (10)$$

Figure B4 shows the seasonal change of thickness difference between ULS draft and IJIS draft calculated using equations (9) and (10). The thickness difference for all years and all mooring points plotted together show significant seasonal variability with minima in January and September. Underestimation error increases toward summer and causes a maximum in June. Overestimation error increases toward late autumn and causes a maximum in October. This suggests that existence of surface liquid water and surface salt drainage in summer and refreezing melt water contribute to large signal shifts on microwave radiation. *Smith* [1998] suggested that melting and refreezing can be detected from a combination of 19 GHz and 37 GHz of SSM/I due to signal shift. Although this phenomenon seems to be caused also by snow and summer melt, more discussion is needed to solve this problem.

To minimize the seasonal error empirically, the following equation was applied:

$$\text{Modified IJIS draft} = \text{IJIS draft} - (a \cdot JD^4 + b \cdot JD^3 + c \cdot JD^2 + d \cdot JD + e) \quad (11)$$

where JD is Julian Day, $a = -2.09 \times 10^{-9}$, $b = 1.41 \times 10^{-6}$, $c = -2.60 \times 10^{-4}$, $d = 8.56 \times 10^{-3}$, and $e = -0.18$.

Figure B5 indicates a time series of ULS draft (light blue bar) and modified IJIS draft (black dots). Although there are still some differences and offsets, the modified IJIS draft estimates are significantly improved. Further refinements are needed to better constrain the relationships and uncertainties, but the results are sufficient for first-order analysis. Figure B6 presents examples of ice draft distribution calculated by AMSR-E with the modified IJIS draft algorithm.

Acknowledgments

We are deeply indebted to the Captains, officers, and crews of the *CCGS Louis S. St-Laurent* for their undaunted efforts in completing our ambitious Canada Basin expeditions. We are also extremely grateful to Sarah Zimmermann, John Kemp, and Kris Newhall for their contributions to the JOIS cruises and BGOS project. John Toole contributed valuable advice on methods, and the manuscript was greatly improved based on recommendations provided by the reviewers. The Ice-Tethered Profiler data were collected and made available by the Ice-Tethered Profiler Program based at the Woods Hole Oceanographic Institution (http://www.whoi.edu/itp). Support for Krishfield, Proshutinsky, and Timmermans, partial financial support of logistics, hydrographic observations on the board of Canadian icebreaker, and full financial coverage of all mooring instrumentation was provided by the National Science Foundation (under grants OPP-0230184, OPP-0424864, ARC-0722694, ARC-0806306, ARC-0856531, ARC-1107277, and ARC-1203720), and Woods Hole Oceanographic Institution internal funding. Any opinions, findings, and conclusions or recommendations expressed in this publication are those of the authors and do not necessarily reflect the views of the National Science Foundation. Funding for Tateyama was provided by the International Arctic Research Center – Japan Aerospace Exploration Agency (IJIS) Arctic project, and for Williams, Carmack, and McLaughlin by Fisheries and Oceans Canada.

References

Barber, D. G., and J. M. Hanesiak (2004), Meteorological forcing of sea ice concentrations in the southern Beaufort Sea over the period 1979 to 2000, *J. Geophys. Res.*, *109*, C06014, doi:10.1029/2003JC002027.

Barber, D. G., R. Galley, M. G. Asplin, R. De Abreu, K. Warner, M. Pućko, M. Gupta, S. Prinsenberg, and S. Julien (2009), Perennial pack ice in the southern Beaufort Sea was not as it appeared in the summer of 2009, *Geophys. Res. Lett.*, *36*, L24501, doi:10.1029/2009GL041434.

Billeness, D., D. Fissel, E. Ross, D. Lemon, and K. Borg (2004), *ASL IPS Processing Toolbox User's Guide*, Version 1.02 (December 2004), ASL Environ. Services, 111 pp., Sidney, Canada.

Carmack, E., F. McLaughlin, M. Yamamoto-Kawai, M. Itoh, K. Shimada, R. Krishfield, and A. Proshutinsky (2008), Freshwater storage in the Northern Ocean and the special role of the BG, in *Chapter 6 in Arctic-subarctic Ocean Fluxes: Defining the Role of the Northern Seas in Climate*, edited by B. Dickson, J. Meincke, and P. Rhines, pp. 145–170, Springer, New York.

Cavalieri, D. J. (1994) A microwave technique for mapping thin ice, *J. Geophys. Res.*, *99*(C6), 12,561–12,572.

Cavalieri, D. J., P. Gloersen, and W. J. Campbell (1984), Determination of sea ice parameters with the NIMBUS 7 SMMR, *J. Geophys. Res.*, *89*(D4), 5355–5369.

Comiso, J. (2000, updated 2012), *Bootstrap Sea Ice Concentrations from Nimbus-7 SMMR and DMSP SSM/I-SSMIS*, Version 2, Natl. Snow and Ice Data Cent., Boulder, Colo.

Comiso, J. C. (2006), Abrupt decline in the Arctic winter sea ice cover, *Geophys. Res. Lett.*, *33*, L18504, doi:10.1029/2006GL027341.

Comiso, J. C., C. L. Parkinson, R. Gersten, and L. Stock (2008), Accelerated decline in the Arctic sea ice cover, *Geophys. Res Lett.*, *35*, L01703, doi:10.1029/2007GL031972.

Dukhovskoy, D. S., M. A. Johnson, and A. Proshutinsky (2004), Arctic decadal variability: An auto-oscillatory system of heat and freshwater exchange, *Geophys. Res. Lett.*, *31*, L03302, doi:10.1029/2003GL019023.

Farrell, S. L., S. W. Laxson, D. C. McAdoo, D. Yi, and H. J. Zwally (2009), Five years of Arctic sea ice freeboard measurements from the ice, cloud and land elevation satellite, *J. Geophys. Res.*, *114*, C04008, doi:10.1029/2008JC005074.

Fichot, C. G., K. Kaiser, S. B. Hooker, R. M. W. Amon, M. Babin, S. Belanger, S. A. Walker, and R. Benner (2013), Pan-Arctic distributions of continental runoff in the Arctic Ocean, *Sci. Rep.*, *3*, 1053, doi:10.1038/srep01053.

Fowler, C. and M. Tschudi (2003, updated 2013), *Polar Pathfinder Daily 25 km EASE-Grid Sea Ice Motion Vectors*, Version 1, Natl. Snow and Ice Data Cent., Boulder, Colo.

Fukamachi, Y., G. Mizuta, K. I. Oshima, H. Melling, D. Fissel, and M. Wakatsuchi (2003), Variability of sea-ice draft off Hokkaido in the Sea of Okhotsk revealed by a moored ice-profiling sonar in winter of 1999, *Geophys. Res. Lett.*, *30*(7), 1376, doi:10.1029/2002GL016197.

Galley, R. J., E. Key, D. G. Barber, B. J. Hwang, and J. K. Ehn (2008), Spatial and temporal variability of sea ice in the southern Beaufort Sea and Amundsen Gulf: 1980–2004, *J. Geophys. Res.*, *113*, C05S95, doi:10.1029/2007JC004553.

Giles, K. A., S. W. Laxon, and A. L. Ridout (2008), Circumpolar thinning of Arctic sea ice following the 2007 record ice extent minimum, *Geophys. Res. Lett.*, *35*, L22502, doi:10.1029/2008GL035710.

Giles, K. A., S. W. Laxon, A. L. Ridout, D. J. Wingham, and S. Bacon (2012), Western Arctic Ocean freshwater storage increased by wind-driven spin-up of the Beaufort Gyre, *Nat. Geosci.*, *5*, 194–197, doi:10.1038/NGEO1379.

Hansen, E., S. Gerland, M. A. Granskog, O. Pavlova, A. H. H. Renner, J. Haapala, T. B. Løyning, and M. Tschudi (2013), Thinning of Arctic sea ice observed in Fram Strait: 1990–2011, *J. Geophys. Res.*, *118*, 5202–5221, doi:10.1002/jgrc.20393.

Kimura, N. and M. Wakatsuchi (1999), Processes controlling the advance and retreat of sea ice in the Sea of Okhotsk, *J. Geophys. Res.*, *104*(C5), 11,137–11,150.

Krishfield, R., J. Toole, A. Proshutinsky, and M. -L. Timmermans (2008), Automated ice-tethered profilers for seawater observations under pack ice in all seasons, *J. Atmos. Ocean. Technol.*, *25*, 2091–2095, doi:10.1175/2008JTECHO587.1.

Kovacs, A. (1996), Sea Ice Part 1. Bulk Salinity versus ice floe thickness, *CRREL Rep. 96-7*, U.S. Army Cold Regions Research and Engineering Laboratory, Hanover, N. H.
Kwok, R. (2008), Outflow of Arctic sea ice into the Greenland and Barents Seas: 1979–2007, *J. Clim.*, *22*(9), 2438–2457, doi:10.1175/2008JCLI2819.1.
Kwok, R., and G. F. Cunningham (2010), Contribution of melt in the Beaufort Sea to the decline in Arctic multiyear sea ice coverage: 1993–2009, *Geophys. Res. Lett.*, *37*, L20501, doi:10.1029/2010GL044678.
Kwok, R., G. F. Cunningham, H. J. Zwally, and D. Yi (2007), Ice, Cloud, and land Elevation Satellite (ICESat) over Arctic sea ice: Retrieval of freeboard, *J. Geophys. Res.*, *112*, C12013, doi:10.1029/2006JC003978.
Kwok, R., G. F. Cunningham, M. Wensnahan, I. Rigor, H. J. Zwally, and D. Yi (2009), Thinning and volume loss of the Arctic Ocean sea ice cover: 2003–2008, *J. Geophys. Res.*, *114*, C07005, doi:10.1029/2009JC005312.
Kwok, R., G. F. Cunningham, S. S. Manizade, and W. B. Krabill (2012), Arctic sea ice freeboard from IceBridge acquisitions in 2009: Estimates and comparisons with ICESat, *J. Geophys. Res.*, *117*, C02018, doi:10.1029/2011JC007654.
Laxon, S. W., et al. (2013), CryoSat-2 estimates of Arctic sea ice thickness and volume, *Geophys. Res. Lett.*, *40*, 732–737, doi:10.1002/grl.50193.
Laxon, S., N. Peacock, and D. Smith (2003), High interannual variability of sea ice thickness in the Arctic region, *Nature*, *425*(6961), 947–950.
Lindsay, R. W., and J. Zhang (2005), The thinning of Arctic sea ice, 1988–2003: Have we passed a tipping point?, *J. Clim.*, *18*, 4879–4894.
Martin, S., R. Drucker, and K. Yamashita (1998), The production of ice and dense shelf water in the Okhotsk Sea polynyas, *J. Geophys. Res.*, *103*, 27,771–27,782.
Martin, S., R. Drucker, R. Kwok and B. Holt (2004), Estimation of the thin ice thickness and heat flux for the Chukchi Sea Alaskan coast polynya from Special Sensor Microwave/Imager data, 1990–2001, *J. Geophys. Res.*, *109*, C10012, doi:10.1029/2004JC002428.
McNeill, J. D. (1980), Electromagnetic terrain conductivity measurements at low induction numbers, Technical Note, TN-6, 15 pp., Geonics Ltd., Mississauga, Canada.
McLaughlin, F. A., and E. Carmack (2010), Deepening of the nutricline and chlorophyll maximum in the Canada Basin interior, 2003–2009, *Geophys. Res. Lett.*, *37*, L24602, doi:10.1029/2010GL045459.
McLaughlin, F., et al. (2010), Physical, chemical and zooplankton data from the Canada Basin, August 2003, *Can. Data Rep. Hydrogr. Ocean Sci*. 184, ix + 303 pp, Fisheries and Oceans, Canada, Sidney, B. C.
Melling, H., and D. A. Riedel (1995), The underside topography of sea ice over the continental shelf of the Beaufort Sea in the winter of 1990, *J. Geophys. Res.*, *100*(C7), 13,641–13,653.
Melling, H., P. H. Johnston, and D. A. Riedel (1995), Measurements of the underside topography of sea ice by moored subsea sonar, *J. Atmos. Oceanic Technol.*, *12*, 589–602.
Melling, H., and D. A. Riedel (1996), Development of the seasonal pack ice in the Beaufort Sea during the winter of 1991-92: A view from below, *J. Geophys. Res.*, *101*(C5), 11,965–11,991.
Melling, H., D. A. Riedel, and Z. Gedalof (2005), Trends in the draft and extent of seasonal pack ice, Canadian Beaufort Sea, *Geophys. Res. Lett.*, *32*, L24501, doi:10.1029/2005GL024483.
Morison, J., R. Kwok, C. Peralta-Ferriz, M. Alkire, I. Rigor, R. Andersen and M. Steele (2012), Changing Arctic Ocean freshwater pathways, *Nature 481*, 66–70, doi:10.1038/nature10705.
Moritz, R. E. (1992), Seasonal and regional variability of sea ice thickness distribution, paper presented at 3rd Conference on Polar Meteorology and Oceanography, 29 Sept.−2 Oct., pp. 68–71, Am. Meteorol. Soc., Portland, Oreg.
Moritz, R. E. and A. N. Ivakin (2012), Retrieving sea-ice thickness from ULS echoes: Methods and data analysis, paper presented at 11th European Conference on Underwater Acoustics, 8 pp., Inst. Acoust., St. Albans, U. K.
Overland, J. E., Wang, M., and S. Salo (2008), The recent Arctic warm period, *Tellus, Ser. A*, *60*, 589–597.
Parkinson, C. L. and D. J. Cavalieri (2008), Arctic sea ice variability and trends, 1979–2006, *J. Geophys. Res.*, *113*, C07003, doi:10.1029/2007JC004558.
Parkinson, C. L. and J. C. Comiso (2013), On the 2012 record low Arctic sea ice cover: combined impact of Preconditioning and an August Storm, *Geophys. Res. Lett.*, *40*, 1356–1361, doi:10.1002/grl.50349.
Perovich, D. K., J. A. Richter-Menge, K. F. Jones, and B. Light (2008), Sunlight, water, and ice: Extreme Arctic sea ice melt during summer of 2007, *Geophys. Res. Lett.*, *35*, L11501, doi:10.1029/2008GL034007.
Proshutinsky, A., and M. Johnson (1997), Two circulation regimes of the wind-driven Arctic Ocean, *J. Geophys. Res.*, *102*, 12,493–12,514.
Proshutinsky, A., Bourke, R. H., and F. A. McLaughlin (2002), The role of the BG in Arctic climate variability: seasonal to decadal climate scales, *Geophys. Res. Lett.*, *29*(23), 2100, doi:10.1029/2002GL015847.
Proshutinsky, A., R. Krishfield, M.-L. Timmermans, J. Toole, E. Carmack, F. McLaughlin, W. J. Williams, S. Zimmermann, M. Itoh, and K. Shimada (2009), The BG freshwater reservoir: State and variability from observations, *J. Geophys. Res.*, *114*, C00A10, doi:10.1029/2008JC005104.
Proshutinsky, A., et al. (2012), The Arctic, j. Ocean [in "State of the Climate in 2011"], *Bull. Am. Meteorol. Soc.*, *93*(7), S158–S163.
Reid, J. E., and J. Vrbancich (2004), A comparison of the inductive-limit footprints of airborne electromagnetic systems, *Geophysics*, *69*, 1229–1239.
Reid, J. E., A. P. Worby, J. Vrbancich, and A. I. S. Munro (2003), Ship-borne electromagnetic measurement of Antarctic sea-ice thickness, *Geophysics*, *68*, 1537–1546.
Smith, D. M. (1998), Observation of perennial Arctic sea ice melt and freeze-up using passive microwave data, *J. Geophys Res.*, *103*(C12), 27,753–27,769.
Strass, V. H. (1998), Measuring sea ice draft and coverage with moored upward looking sonars, *Deep Sea Res., Part I*, *45*, 795–818.
Stroeve, J. C., M. C. Serreze, M. K. Holland, J. E. Kay, J. Maslanik, and A. P. Barrett (2012), The Arctic's rapidly shrinking sea ice cover: A research synthesis, *Clim. Change*, *110*, 1005–1027, doi:10.1007/s10584-011-0101-1.
Tamura, T., K. I. Ohshima, T. Markus, D. J. Cavalieri, S. Nihashi, and N. Hirasawa (2007), Estimation of thin ice thickness and detection of fast ice from SSM/I data in the Antarctic Ocean, *J. Atmos. Ocean. Tech.*, *24*, 1757–1772.
Tateyama, K., H. Enomoto, T. Toyota, and S. Uto (2002), Sea ice thickness estimated from passive microwave radiometers, *Polar Meteorol. Glaciol.*, *16*, 15–31.
Tateyama, K., K. Shirasawa, S. Uto, T. Kawamura, T. Toyota, and H. Enomoto (2006), Standardization of electromagnetic-induction measurements of sea ice thickness in polar and subpolar seas, *Ann. Glaciol.*, *44*, 240–246.
Tateyama, K., R. A. Krishfield, W. J. Williams, and H. Enomoto (2013), Estimation of Arctic sea ice thickness from satellite passive microwave radiometers, paper presented at 3rd International Symposium on the Arctic Research (ISAR-3), Tokyo, Japan, 14–17 January. [Available at http://www.jcar.org/isar-3/abstracts/S6_oral.pdf.].

Timco, G. W., and R. M. W. Frederking (1996), A review of sea ice density, *Cold Reg. Sci. Technol.*, *24*, 1–6.
Toole, J. M., R. A. Krishfield, M.-L. Timmermans and A. Proshutinsky (2011), The ice-tethered profiler: Argo of the Arctic, *Oceanography*, *24*(3), 126–135, doi:10.5670/oceanog.2011.64.
Ulaby, F. T., R. K. Moore, and A. K. Fung (1982), *Microwave Remote Sensing, Active and Passive-*, Vol. II - Radar Remote Sensing and Surface Scattering and Emission Theory, 609 pp., Artech House, Inc., Dedham, Mass.
Uto, S., H. Shimoda, and S. Ushio (2006), Characteristics of sea ice thickness and snow-depth distributions of the summer landfast ice in Lützow-Holm Bay, east Antarctica, *Ann. Glaciol.*, *44*, 281–287.
Vellinga, M., B. Dickson, and R. Curry (2008), The Changing view on how freshwater impacts the Atlantic meridional overturning circulation, in *Arctic-Subarctic Ocean Fluxes: Defining the Role of the Northern Seas in Climate*, edited by R. R. Dickson, J. Meincke, and P. Rhines, pp. 289–314, Springer, N. Y.
Wadhams, P. and R. J. Horne (1980), An analysis of ice profiles obtained by submarine sonar in the Beaufort Sea, *J. Glaciol.*, *25*(93), 401–424.
Wadhams, P., N. Hughes, and J. Rodrigues (2011), Arctic sea ice thickness characteristics in winter 2004 and 2007 from submarine sonar transects, *J. Geophys. Res.*, *116*, C00E02, doi:10.1029/2011JC006982.
Williams, W. (2010), Report on the Oceanographic Research Conducted aboard the CCGS Louis S, 15 Sept.−15 Oct., Joint Ocean Ice Study (JOIS) 2010 cruise report., 60 pp., Fish. and Oceans Can., St.-Laurent.
World Meteorological Organization (1970), WMO Sea ice Nomenclature, *WMO Series 259*, Geneva.
Yamamoto-Kawai, M., F. A. McLaughlin, E. C. Carmack, S. Nishino, and K. Shimada (2008), Freshwater budget of the Canada Basin, Arctic Ocean, from salinity, $\delta^{18}O$, and nutrients, *J. Geophys. Res.*, *113*, C01007, doi:10.1029/2006JC003858.
Yamamoto-Kawai, M., F. A. McLaughlin, E. C. Carmack, S. Nishino, K. Shimada, and N. Kurita (2009), Surface freshening of the Canada Basin, 2003–2007: River runoff versus sea ice meltwater, *J. Geophys. Res.*, *114*, C00A05, doi:10.1029/2008JC005000.